Advances in High-Z semiconductor radiation detectors at BNL

G. Pinaroli[1]*, A. E. Bolotnikov[1], M. Bouckicha[1], F. Capocasa[1], L. Cultrera[1], A. K. Rumaiz[2], E. Tamura[1] and G. A. Carini[1]

[1]Instrumentation Department, Brookhaven National Laboratory, Upton, NY, United States, [2]NSLS-II, Brookhaven National Laboratory, Upton, NY, United States

Semiconductor radiation detectors play a crucial role in scientific research and technological applications, with materials typically categorized as low- or high-Z depending on their atomic numbers and densities. This distinction is not strictly defined because the selection of materials depends on the specific application and the energy range. Low-Z semiconductors such as diamond, silicon (Si), selenium (Se), and silicon carbide (SiC) are widely used in X-ray and charged particle detection due to their excellent charge transport properties and radiation hardness. High-Z semiconductors, including germanium (Ge) and compound materials such as cadmium telluride (CdTe), cadmium zinc telluride (CdZnTe or CZT), and emerging lead halide perovskites (most promising is CsPbBr3), offer absorption efficiency in the hard X-ray and gamma-ray regions comparable to CZT. These materials enable advancements in diverse fields, including biology, astrophysics, medical imaging, and industrial inspection. At Brookhaven National Laboratory (BNL), the Instrumentation Department is at the forefront of developing cutting-edge semiconductor detector technologies to address the evolving needs of fundamental and applied research. The projects cover the entire development cycle, from the investigation of new materials and optimization of detector architectures to the design of low-noise readout electronics and signal processing techniques. The ongoing research projects focus on next-generation detection systems that improve sensitivity, energy resolution, and robustness for a wide range of applications. The continuous demand for versatile and high-performance detector systems drives research in multiple directions with emphasis on advancing detector integration within complex experimental requirements, ensuring seamless compatibility with large-scale scientific facilities, and developing scalable and cost-effective fabrication techniques. The combination of novel materials, innovative detector designs, and state-of-the-art readout electronics paves the way for next-generation semiconductor detectors with unprecedented performance. In this work, we present an overview of our recent advances in semiconductor detectors and their applications.

KEYWORDS

X-and gamma-ray detectors, radiation detectors, CdZnTe, TlBr, CsPbBr3, high-purity germanium detectors, a-Se

1 Introduction

Among the various types of ionizing radiation, X-rays and gamma rays play important roles in our daily lives. From scientific research and medical diagnostics to industrial imaging and portal security, photon detection serves as a fundamental tool for, i.e., uncovering nuclear processes, visualizing the internal structures of objects, defining elemental composition of matter and many others. The broad range of applications involving X-ray and gamma-ray detection often requires radiation detectors with diverse and specialized properties. These changing demands drive the ongoing development of novel, advanced detectors capable of processing large volumes of data and conducting multiple types of measurements with precision and efficiency. Simultaneously, rapid advancements in science and technology continue to unlock new challenges and applications—many of which were previously unimaginable.

Semiconductor detectors exemplify the innovation occurring in radiation detection. Their development has closely followed the evolving needs of modern applications. High-Z semiconductor detectors, for instance, are essential in synchrotron radiation facilities, where efficient photon absorption is critical. Room-temperature semiconductors such as Cadmium Telluride (CdTe) and Cadmium-Zinc-Telluride (CZT) are increasingly used in medical imaging and nuclear nonproliferation efforts, offering portability and high-resolution capabilities. Novel point-contact high-purity germanium (HPGe) detectors have enabled precise measurements in rare event searches like neutrinoless double-beta decay experiments. Additionally, perovskite-based detectors are emerging as promising candidates for low-cost, large-area detector arrays, particularly for X-ray imaging applications.

Semiconductor detectors operating in charge-collecting mode provide high energy and position resolution resolutions, and robust and versatile designs in a broad field of applications. Their main advantage, in comparison to gas- or liquid-filled detectors, are low energies required to produce electron-hole pairs and fast charge collection. For a given absorbed energy, semiconductor detectors generate a much greater number of charge carriers ensuring the high signal-to-noise ratio and high energy resolution. Furthermore, semiconductor detectors take advantages of the semiconductor industry's fabrication and integration processes, including microelectronics enabling the development of detectors with thousands of channels for various applications (Ohsugi et al., 2005; Abdesselam et al., 2006).

The continuous advancement in technology and the growing need for precise radiation detection have driven significant innovation in detector materials and designs. Semiconductor detectors, particularly silicon-based ones, have long been favored due to their well-established fabrication processes aided by progress in microelectronics industries, high charge collection efficiency, and scalability. Silicon detectors excel in charged particle detection and low-energy X-ray applications, but their relatively low atomic number limits their efficiency in detecting high-energy photons. Different semiconductor materials can be used for radiation detection for high-energy X-rays, and the method of the signal readout depends on the material properties. In wide bandgap materials such as diamond, thallium bromide (TlBr), CdTe, and CZT, the intrinsic carrier concentration is low at room temperature (Knoll, 2010). In contrast, low bandgap semiconductors like silicon (Si) and germanium (Ge) require blocking contacts or cooling to deplete the material. Detection efficiency is influenced by material density and atomic number and device thickness. For instance, silicon detectors typically operate in the 1–30 keV range, whereas germanium, TlBr, CdTe, CZT and $CsPbBr_3$ detectors can be extended to the MeV range.
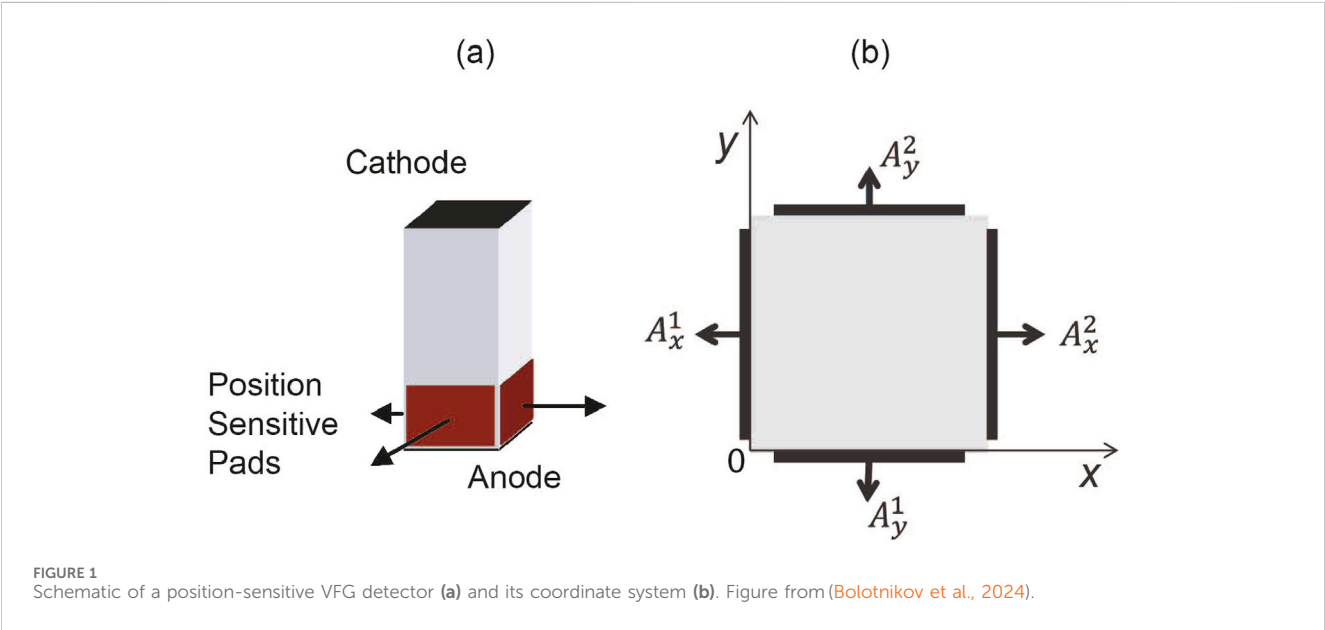
These High-Z semiconductors detector are primarily of interest in X- and γ-ray detectors in a broad area of applications from nuclear physics and astronomy to medical and industrial imaging. Representative examples are: CZT detectors play major roles in modern CT and SPECT systems for medical imaging. Arrays of CZT detectors were proposed for γ-ray astronomy and double beta decay search (COBRA). TlB and $CsPbBr_3$ are emerging materials that will eventually replace CZT in some applications requiring compact instruments with high detection efficiency or large area low-cost arrays. HPGe detectors are used in many practical applications for γ-ray spectroscopy and recently in fundamental science experiments such as dark and double beta decay search (Majorana, GERDA, LEGENS). Table 1 summarizes the main material parameters of interest for radiation detector sensors.

2 Position-sensitive virtual frisch-grid detectors (VFG) for imaging and spectroscopy of gamma-ray

CZT and TlBr semiconductors are known for their high photon attenuation, low leakage currents, room temperature stability, and high spectral performance. CZT is undoubtedly a champion material today, but others, such as TlBr and CsPbBr3 (reported in Section 5), are currently emerging alternative materials suitable in many applications. There are several popular detector configurations optimized for specific applications. Among them are pixelated, virtual Frisch-grid, coplanar-grid (CPG) and hemispherical detectors are most widely used (Knoll, 2010). Despite a variety of the designs, all of them operate as virtual-Frisch grid detectors in which the Frisch-grid effect (Frish, 1948) (electrostatic shielding) is achieved by using particular contacts geometries. For example, in pixel detectors, the charge is collected on one pixel, while the rest of the virtually grounded pixels act as a shielding electrode. Historically, the BNL team has focused on the development of virtual Frisch-grid detectors. The position-sensitive virtual Frisch-grid (VFG) detectors have been proposed to maximize the performance of large-volume bar-shaped detector crystals with long-drift lengths. Achieving the high 3D position resolution is critical for enhancing the spectral and imaging performance of these detectors, which operate in a time-projection chambers (TPC) mode (Nygren, 1975). The crystal geometry and detector design offer cost-effective integration of large-area arrays, as well as the flexibility to scale both the quantity and size of the crystals, resulting in high sensitivity and better imaging. With 3D position sensitivity, we address the non-uniformity in detector response, presenting a solution to one of the major technological challenges that limit the use of large-

TABLE 1 Key properties of the presented detector materials evaluated at room temperature.

Material	Resistivity ($\Omega \cdot$ cm)	μ_e (cm²/V. s)	μ_h (cm²/V. s)	$\mu\tau$ (cm²/V)
CZT (Szeles, 2004)	~1 × 10¹⁰	1,000	50	~5 × 10⁻³
TlBr (Dönmez et al., 2012)	~3 × 10¹¹	25	10	~1 × 10⁻⁴
HPGe (Luke and Amman, 2007)	~5 × 10¹⁰	3,900	1900	~1
CsPbBr₃ (He et al., 2019)	~1 × 10⁹	~60	~50	~1 × 10⁻³

FIGURE 1
Schematic of a position-sensitive VFG detector **(a)** and its coordinate system **(b)**. Figure from (Bolotnikov et al., 2024).

thickness and volume detectors in practical applications. Arrays of position sensitive VFG detectors is an economical way to integrate large area position sensitive γ-ray detectors for imaging and spectroscopy where the applications of interest are γ-ray astronomy, non-proliferation and nuclear security, safeguards, and medical imaging. Energy range of interest typically is from ~20 keV up to 50 MeV. It is worth mentioning that CZT detectors have strong radiation resistance and are expected to be able to operate in a Low Earth Orbit passing daily through the South Atlantic Anomaly radiation belt where the onboard instruments are exposed to high fluxes of highly-ionizing non-relativistic protons on low-altitude earth orbits for years (Bolotnikov et al., 2022). We have investigated the feasibility of using arrays of long-drift large-volume CZT detectors in space telescopes operating in low Earth orbits. We employed the proton beam at the NASA Space Radiation Laboratory with energies of 100 and 150 MeV to irradiate four 8 × 8 × 32 mm³ detectors. No polarization effects were observed as the detectors were irradiated by protons with fluxes up to 160 p/cm²/s for several hours. We observed small (<2%) shifts of the peak positions after proton exposure up to 4 × 10⁷ p/cm² due to radiation damage, which can be corrected using in orbit calibrations. Such a radiation dose could be expected during a 5-year mission. The detectors stopped responding to gamma radiation completely after receiving the extremely high dose of ~10¹⁰ p/cm².

2.1 Position-sensitive virtual frish-grid detector (VFG)

The VFG design has been proposed for radiation detectors operating a single-type-carrier collection mode, meaning that only one polarity carrier, electrons or holes, has substantially higher mobility and lifetime compared to the other carrier type, and therefore generates strongest signals in the devices (Knoll, 2010). A drawback of the single-type-carrier mode is that the output signals strongly depend on the locations of interaction sites, which degrades the spectral resolution since the interaction sites are typically randomly distributed over the detector volume. The VFG is one of the designs proposed to overcome this effect in detectors using different detecting media, including room-temperature semiconductors. The Frisch grid–an electron-transparent metal grid–was originally proposed for gas ionization chambers and used for electrostatically shielding the anodes from the slow-moving positive ions (Bunemann et al., 1949). For semiconductor detectors, the same shielding effect can be achieved by placing the grounded electrodes outside of the detector volume, e.g., on the crystal's side surfaces like in our design. Figure 1 depicts the schematic of the VFG configuration and its coordinate system.

The BNL team optimized the position and geometry of the shielding electrode (Bolotnikov et al., 2006; Polack et al., 2010). Figure 2 shows examples of the induced charge signal captured from
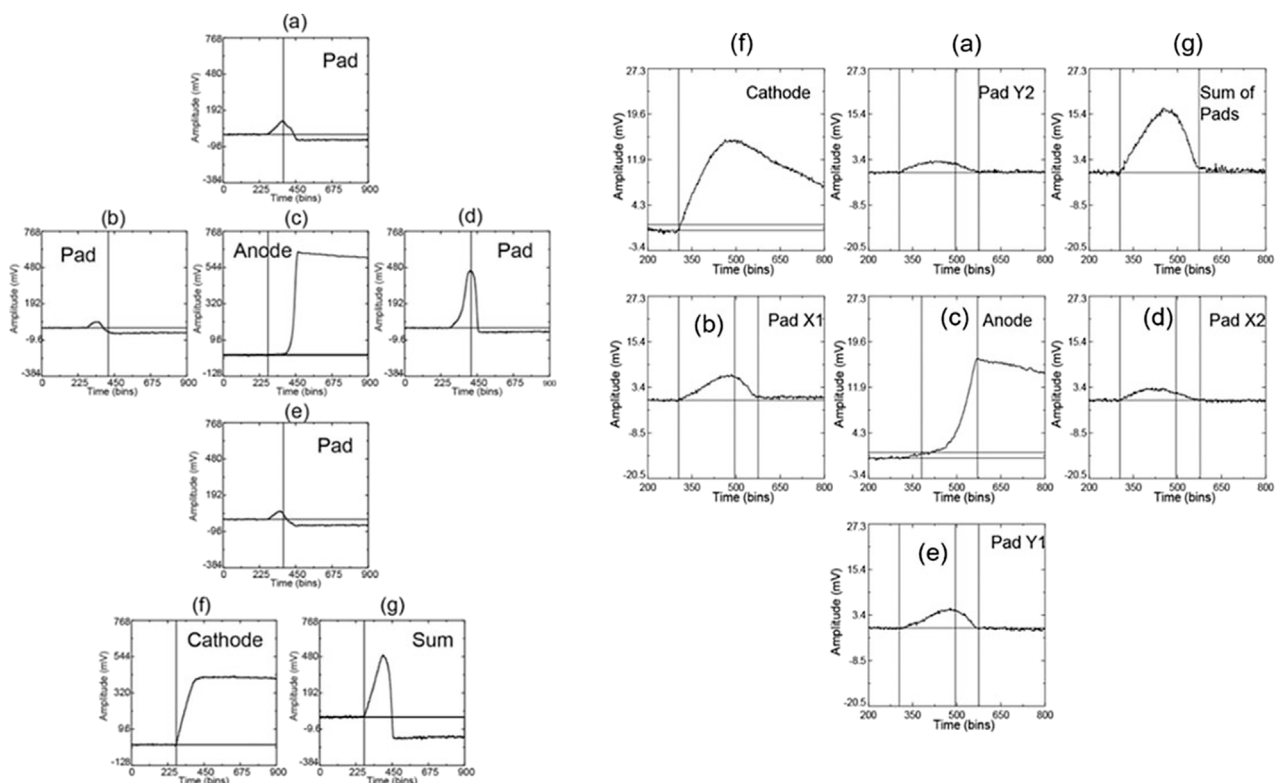
FIGURE 2
Waveforms captured from an $8 \times 8 \times 32$ mm^3 CZT (left) and $5 \times 5 \times 12$ mm^3 (right) TlBr detectors: cathode **(f)**, the anode **(c)**, and four pads **(a,b,d,e)**. Plot **(g)** represents the sum of the pad signals. The solid vertical lines indicate the moment when the interaction occurs (evaluated using the cathode signal or the sum of the pad signals) and the moment when synchronized pad samples were selected (Bolotnikov et al., 2020; Kargar et al., 2021). In addition, the rightmost lines on the TlBr plots indicates the moment when carriers reach the anode (evaluated based on the anode signal).

the pads (a), (b), (d), and (e), while the plot (g) represents the sum of the pad signals, P, measured with $8 \times 8 \times 32$ mm^3 CZT (left) and $5 \times 5 \times 12$ mm^3 TlBr detectors (Bolotnikov et al., 2020; Kargar et al., 2021). Plots (c) and (f) show the anode, A, and the inverted cathode signals, C. As seen from the plots (f) and (g), the leading edge of the sum of the pad signals is almost identical to the leading edge of the cathode signal, which means that the former can be used to substitute for the cathode signals.

The interaction occurrence moment is measured based on the cathode signal by using linear interpolation of the rising front. However, the event trigger time is generated based on the anode signal when it crosses the threshold level. The solid vertical lines in the plots indicate the occurrence time of the event being identified using the cathode signal or the sum of the pad signals (whichever has the strongest amplitude). The cathode and anode amplitudes have different polarities, but the same range of amplitudes. The pad signals rise as the electron cloud reaches the pads and decay to their minimum levels when the cloud reaches the anode. These levels could be negative for interaction sites close to the anode due to inefficiency of shielding. We note that the pads reach their maximum at slightly different times and different positions with respect to the anode, which means that if these maxima are used for estimating the X-Y coordinate, this will introduce systematic fluctuations. A better approach is to use synchronized samples taking from the pad waveforms just after they reach their maximum. Either shaped signals (shaping amplifier) or sampled

induced charge waveforms could be used to evaluate the pad amplitudes with respect to their negative levels. However, the shaping does not preserve timing information. The sum of the positive peaks of the pad signals, measured with respect to their baseline levels, is equivalent to the cathode signal. Therefore, either the C/A or P/A can be used to evaluate the Z coordinate. The carrier's drift time can be used as well to independently estimate Z coordinates. The advantage of adding the charge-sensing pads that enable the 3D position sensitivity is that it allows the correction of response inhomogeneity in all three dimensions. In addition, this would increase the acceptance rate of CZT crystals and reduce the cost of the instrument. We call this procedure 3D corrections versus 1D (or interaction-depth) corrections (Bolotnikov et al., 2006). Figure 3 illustrates the sequential improvements of energy resolution after applying 1D and 3D corrections for a $10 \times 10 \times 32$ mm^3 detector biased at 2,200 V. Even at such low bias, the energy resolution can be improved from 3.6% (raw data) to 0.9% FWHM at 662 keV after 3D corrections. In this example, the energy resolution is mainly determined by the electronic noise.

2.2 CZT VFG detector

Figure 4 illustrates the performance of the 4×4 CZT array by showing the pulse-height spectra measured from 232U and 137Cs uncollimated sources (Bolotnikov et al., 2020). It shows 16 energy
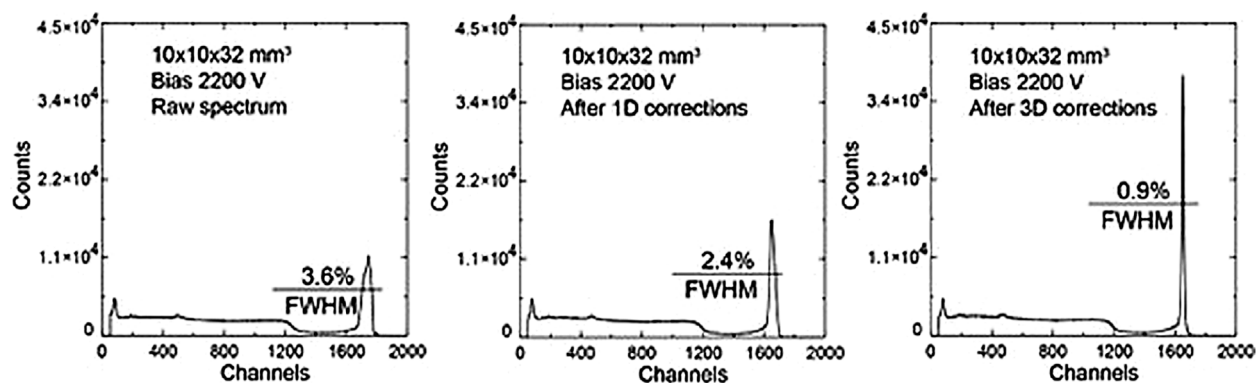
FIGURE 3
The ^{137}Cs spectra after 1D and after 3D corrections for a 10 × 10 × 32 mm^3 CZT detector biased at 2,200 V. Plots from (Bolotnikov et al., 2020).

spectra after 3D corrections measured from 16 detectors biased at 2,800 V at room temperature. The combined spectra after 1D and after 3D corrections are shown in Figures 4b,c, respectively. The energy resolutions evaluated for 286 and 662 keV lines of the 3D corrected spectrum were 1.8% FWHM at 200 keV and <0.9% at 662 keV at 23 °C. In the case of just 1D correction, we obtained 2.8% and 2.5%, respectively. The raw (uncorrected) spectra (not shown) typically resulted in 3%–6% energy resolution range at 662 keV. The main factor limiting the energy resolution of the VFG detectors is electronic noise primarily related to the high leakage current, 3–5 nA, and large anode capacitance (in the order of ~3 pF). In collaboration with NASA Goddard Space Flight Center, BNL developed a prototype of the large-area array of 6 × 6 × 20 mm^3 CZT detectors for the proposed future All-sky Medium Energy Gamma-ray Observatory (AMEGO), which is an Astrophysics Probe mission concept designed to explore the sky in the MeV region (McEnery et al., 2019; Moiseev, 2021). AMEGO will advance new explorations in MeV astrophysics, including spectral studies, polarization, and nuclear line spectroscopy. This energy range is very challenging because of how photons interact with detector materials: both via Compton scattering at lower energy MeV and via pair production at higher energies. Thick and dense detectors are needed to fully contain Compton interactions and a precise measurement of the electron tracks through the instrument volume is needed to reconstruct the original gamma-ray direction. The future array will employ 8 × 8 × 32 mm^3 position-sensitive VFG bars. The thickness of these detectors is maximized since the interaction depth for Compton scattering is ~10 g/cm^2 at 1 MeV. With only six channels per bar, this readout gives excellent energy resolution of <1% FWHM at 1 MeV and position resolution of ~1 mm in all three dimensions. Figure 5 shows the designed prototype.

2.3 TlBr VFG detector

TlBr continue to be a promising candidate for high-energy resolution semiconductor gamma-ray detectors (Hitomi et al., 1999; Nogami et al., 2023; Churilov et al., 2010). Because of its high atomic number (Tl = 81, Br = 35), high density (7.56 g/cm^3),

and relatively low melting temperature (460 °C), TlBr combines the three most competitive features of gamma-ray detectors: high detection efficiency, good energy resolution, and low fabrication cost, which makes the material particularly attractive in applications that require small and compact systems, yet highly sensitive to gamma rays. Despite the encouraging results of many researchers, practical implementations of these detectors have proven more challenging than expected, prompting further studies to understand the material and fabrication-related factors limiting device performance and longevity. Using arrays of TlBr bars instead of large crystals is a cost-effective approach for integrating large area/volume detectors. The production yield of high-quality TlBr is a limiting factor, especially for larger single crystals. Employing an array of position-sensitive TlBr detectors can achieve the same or even better performance in the effective area and sensitivity with smaller, generally less expensive[1], crystals compared to CZT. Additionally, arrays of smaller crystals can be scaled more efficiently to cover larger areas and volumes. This approach gives greater flexibility in designing and configuring the detectors to meet specific requirements. Finally, arrays of bars allow for modular design and replacement; if one bar fails or under-performs, it can be replaced without impacting the entire system.

We have characterized over a hundred 5 × 5 × 12 mm^3 detectors fabricated by RMD (https://www.rmdinc.com/) for the 4 × 4 array prototype (Figure 6) to be used in the Radioisotope Identification Device (RIID) – a lightweight, compact, low-power, handheld system that integrates the TlBr detectors with application specific readout circuit (ASIC) based readout electronics and signal processing (Kargar et al., 2021). γ-ray energies of interest for this application are nuclear gamma-ray lines in the range of 100 keV to ~3 MeV.

As was previously explained, the 3D corrections exploit the correlation between response variations caused by crystal defects and their locations inside the detector. However, if charge losses do not correlate with the centroid coordinates of the charges created by

---

1 Estimate based on a comparison of the complexity of the growth equipment, growth and purification procedures.
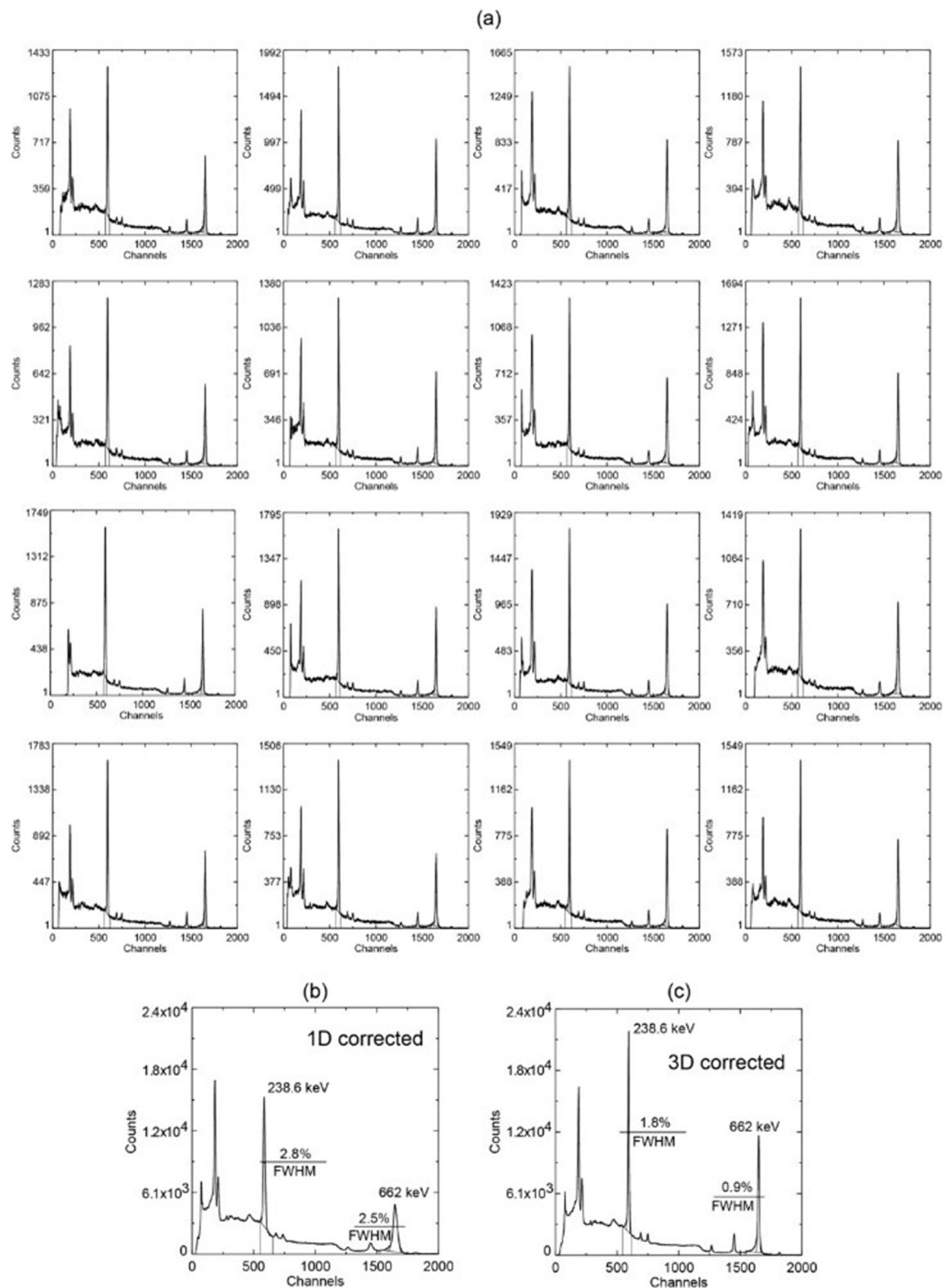
FIGURE 4
Pulse-height spectra measured from ^{232}U and ^{137}Cs uncollimated sources with the 4 × 4 array module: (a) spectra measured from 16-detectors after 3D corrections, (b) the combined spectra after 1D and (c) after 3D corrections. Plots from (Bolotnikov et al., 2020).
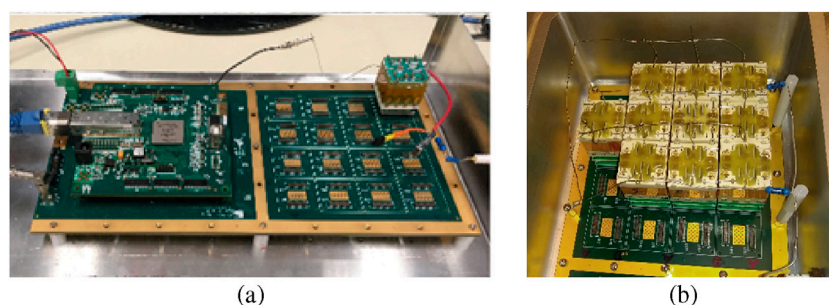
FIGURE 5
(a) A 256-detector benchtop prototype for testing readout ASICs and CZT modules before integrating a flight instrument. **(b)** Motherboard populated with 10 CZT modules. Design concept from (Valverde et al., 2023).

FIGURE 6
TlBr crystals with electrodes, and packaged VFG TlBr detectors with 3D drawing model. The TlBr ingots were grown by RMD using the zone melting technique. The bars were cut, polished, and etched in a bromine-methanol solution. The longest dimension of the device aligns with, or is parallel to, the growth direction. Platinum contacts were sputtered on the cathode and anode sides.

the interaction event because the position resolution is insufficient to resolve small defects spatially or defect movements, the 3D corrections become less effective and require frequent updating of the correction matrixes. Worth to highlight that after the conditioning of the detector (typically 1–2 days), the correction matrix remains stable until the detector dies.

Figure 7 shows the room-temperature pulse-height spectra measured for a good detector operated at a bias of 1.8 kV: (a) the raw spectrum and (b, c) after 1D and 3D corrections, respectively. After the 3D corrections, the energy resolution improved from 3.1% to 1.6% FWHM at 662 keV with an electronic noise contribution of approximately 0.8%. The electronic noise was measured as the fluctuations of the baseline using a channel at the beginning of the waveform. The resulting noise peak was positioned near the 662 keV photopeak for comparison (c). The electronic noise was evaluated as the FWHM of the noise peak (in channels) and normalized as a percentage of the 662 keV photopeak. Further improvements in energy resolution can be achieved by vetoing events from voxels with poor responses based on proximity to the crystal surface, as illustrated in spectra (d) and (e), which demonstrate that our detectors could ultimately achieve 1% or even better energy resolution. It is noteworthy that spectrum (c) demonstrates a high peak-to-Compton ratio (~20 defined as a ratio between the counts per channel at the peak maximum and near the Compton edge), which is only attainable with high-Z and high-density

detector materials like TlBr. Additionally, the spectra suggest that the poor voxels mainly contribute to the Compton continuum. We have tested over a hundred TlBr detectors and accumulated substantial statistics that allowed for a better understanding of the factors limiting our TlBr detectors' performance and made recommendations for addressing them. Among all the tested detectors, approximately 5% exhibited less than 2% energy resolution (good response detectors), around 70% fell within the 2%–4% (typical response detectors) range, and the remainder had resolution above 5% (poor detectors) (Kargar et al., 2021). Differences in performance between detectors is still associated to the not yet mature growth and fabrication process.

2.4 Considerations

Position-sensitive virtual Frisch-grid detectors are an efficient and economically viable choice to fill a given volume of detector area with less dead space and reasonable integration complexity. Initially, we developed and investigated the feasibility of CZT VFG detectors by integrating and testing prototypes based on the smaller $6 \times 6 \times 20$ mm³ CZT crystals which were commercially available at that time. While the demonstrated performance has been excellent, one of the conclusions from these studies is that larger crystals, which suffer less from edge effects where free carriers may drift towards the side surfaces and get trapped. This would require fewer readout
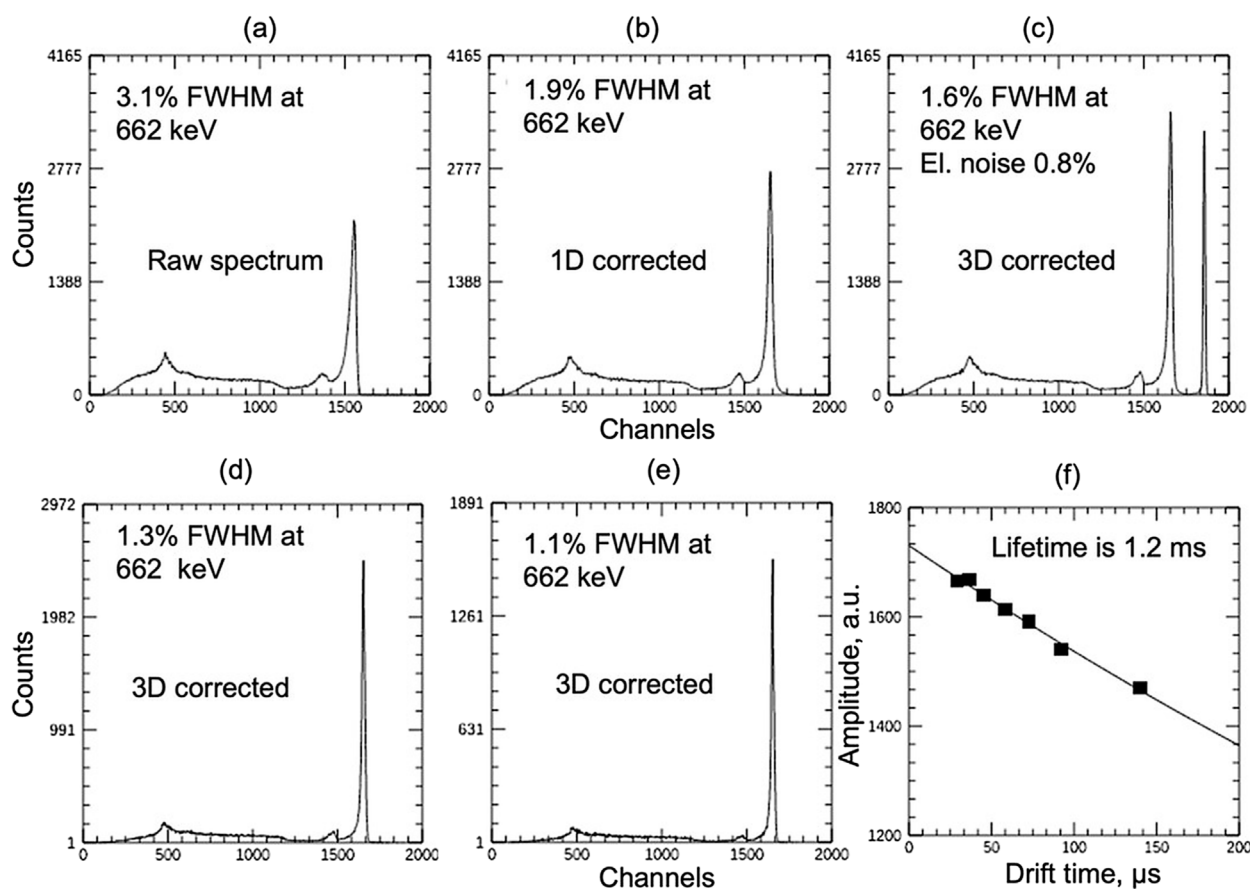
FIGURE 7
Pulse-height spectra measured for a representative good detector: **(a)** raw spectra and **(b,c)** after 1D and 3D corrections, respectively. The peak to the right of the 662 keV photopeak in **(c)** represents the electronic noise of 0.8%. Further improvement of the energy resolution can be achieved by vetoing voxels with poor responses but at the cost of the efficiency losses (reductions of the photopeak counts) seen in spectra **(d,e)**. Plot **(f)** depicts the dependence of the signal amplitudes on drift time, which is used to estimate the electron lifetime.

channels, would be advantageous for this application. Today's CZT detector material make the use of CZT bar-shaped with dimensions up to $15 \times 15 \times 30$ mm^3 possible. Recent advancements in alternative detector materials such as TlBr and CsPbBr$_3$ (test results reported in Section 5.4) open opportunities for using these materials in VFG detectors. High gamma-ray attenuation and low production cost give these materials several competitive features, including high detection efficiency, good energy resolution, and lower fabrication costs, making them suitable for applications requiring compact, highly sensitive gamma-ray detection systems.

3 Germanium detectors for hard X-ray spectroscopy

It is well established that silicon becomes increasingly transparent to X-rays at photon energies above 20 keV, limiting its effectiveness for high-energy applications. As an increasing number of synchrotron beamlines operate in this energy regime, there is a clear need for alternative sensor materials with improved absorption and spectroscopic performance. Germanium presents a compelling solution due to its high atomic number and favorable

charge transport properties. As a monoatomic semiconductor, it also offers well-understood material behavior and consistently high energy resolution, making it ideally suited for spectroscopy at high X-ray energies. While progress has been made in compound semiconductors such as gallium arsenide (GaAs), cadmium telluride (CdTe), for high-energy applications, their relatively poor energy resolution limits their use to applications where resolution is less critical, such as imaging detectors (Eisen et al., 1999). Multi-element high-purity Germanium (HPGe) detectors have also been developed, typically by tiling individual detector elements together and packaging them in a common cryostat. These detectors rely on discrete electronics for readout, which imposes an upper limit on the number of channels that can be practically implemented in an array. While monolithic arrays with up to 100 elements have been developed using discrete-component readout, further advancements will require greater integration of the readout electronics. One of the biggest challenges in the development of Ge is the lack of stable native oxide. Unlike silicon, which utilizes silicon dioxide for pixel isolation in planar processes, germanium presents challenges due to its unstable and hygroscopic oxide. Instead, pixel isolation in Ge detectors has been successfully achieved through trenching, showing promising results.
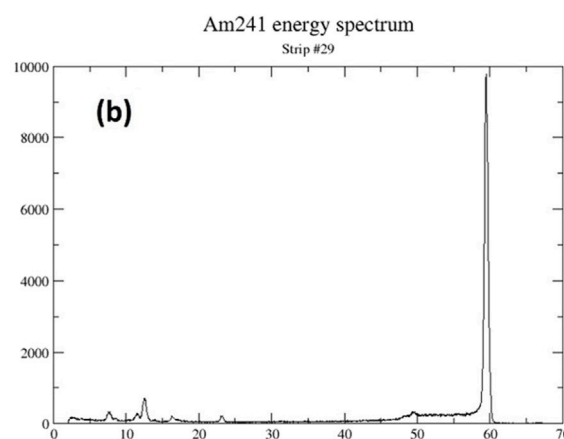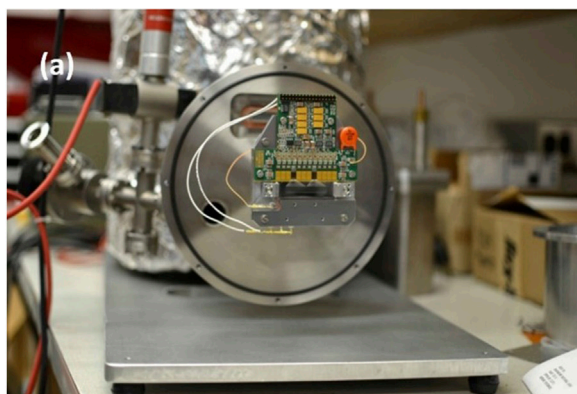
FIGURE 8
(a) Picture of finished 64-strip Germanium detector on liquid N$_2$ dewar. **(b)** Recorded spectrum from 241Am radioactive source.

The fabrication and performance of such detectors are discussed in detail elsewhere (Protic and Riepe, 1985). Briefly, planar germanium detectors are fabricated by diffusing lithium to form an n-type contact, while boron implantation creates a p-type layer on the opposite side. After metal deposition on the p-type side, lithographic patterning is used to create shallow trenches between the pixels. This trenching technique significantly simplifies detector fabrication while improving performance. The first Ge detector system built at BNL using the afore mentioned process was a 64-strip sensor developed HERMES ASIC (Vernon et al., 2019; Rumaiz et al., 2014). This was a collaboration between the detector group at National Synchrotron Light Source (NSLS) II at BNL and Semikon GmbH in Julich, Germany. The detector has 64 pixels, each 0.5 mm by 5 mm, arranged as a series of strips. The ASIC was developed for low-noise photon counting applications where the analog signals can be read by an external multi-channel analyzer (MCA). Figure 8 shows the detector system and the response from 241Am on one of the channels, showing an energy resolution was about 450 eV full width at half maximum (FWHM) (Fano limit (Fano, 1947) at 60 keV for Ge is about 354 eV FWHM). The prototype detector was used to show energy dispersive diffraction (EDX) which requires an energy resolving strip detector to map the volume of the sample illuminated by a white beam (Protic and Riepe, 1985).

Building on the success of the prototype detector system, we developed a program at BNL to fully leverage the sensor's capabilities. The initial readout scheme was simple but required multiplexing to read one channel at a time. To enhance performance, we introduced a new system based on the MARS (Multi-element Amplifier and Readout System) ASIC for subsequent Ge detector development. The MARS ASIC features 32 channels, each equipped with a charge-sensitive preamplifier (offering four programmable gains from 12.5 keV to 75 keV) and a shaping amplifier (with adjustable shaping times from 0.25 μs to 2 μs). Additionally, each channel includes a peak detector and a time-to-analog converter. The ASIC's timing system operates in two modes: measuring time over threshold or determining photon arrival time (Vernon et al., 2020). Since all data from a single ASIC are multiplexed through one differential analog port, photon events are sequentially retrieved by the data acquisition (DAQ) module. The analog timing system records the interval between the photon peak-detect signal and the actual readout. Simultaneously, the DAQ system logs the system clock value. By combining these values, the real-time photon arrival can be reconstructed. The data stream can then be analyzed for time-coincident events in neighboring strips, a key indicator of charge-sharing. Using the MARS ASIC we have developed a variety of 384- and 192-strip detector for X-ray powder diffraction and EDX respectively. Each strip was 125 μm × 8 mm and was read out by MARS ASIC mounted on a closed cycle cryostat. After initial setup, the detector system can be fully maintained by a small ion pump. Figure 9 shows the 384-strip detector system.

X-ray spectroscopy measurements at third-generation synchrotron sources are often limited by the detector system's count rate. Spectroscopy detectors require high energy resolution, as it is crucial for distinguishing closely spaced fluorescence lines in complex spectra. Among high-Z materials, Ge has long been the gold standard for spectroscopic applications. X-ray absorption fine structure spectroscopy (XAFS) is a widely used synchrotron technique for studying atomic and electronic structures (Newville, 2014). XAFS measurements typically involve recording X-ray beam intensity above and below an absorption edge as it passes through a sample. Standard "transmission mode" XAFS experiments use simple ionization chambers. However, for samples with low concentrations or thickness constraints, XAFS data are collected by measuring fluorescence emitted by the sample. For XAFS beamlines, energy-resolving silicon drift detectors are commonly used. However, silicon-based drift sensors become inefficient above 15 keV. In contrast, HPGe detectors provide superior energy resolution and detection efficiency for high-energy X-ray applications.

In addition to the detection scheme and sensor type, detector performance is heavily influenced by front-end electronics. Traditionally, the input transistor of the preamplifier has either been integrated into the sensor itself or wire-bonded to an external low-noise JFET or MOSFET (Bertuccio and Caccia, 2007; De
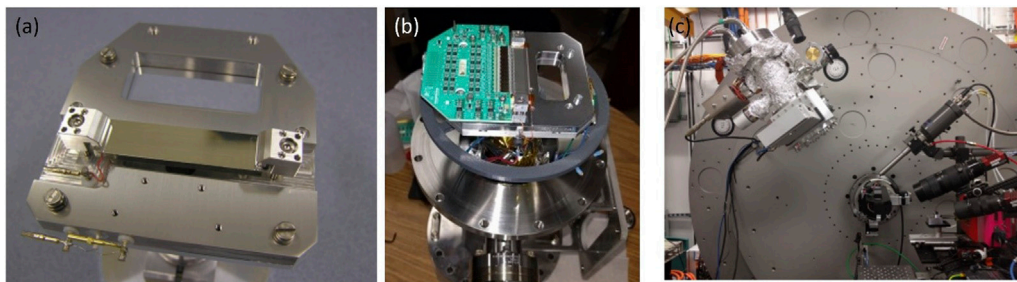
FIGURE 9
(a) 384-strip sensor on cold head. **(b)** Detector mounted on closed cycle refrigerator. **(c)** Detector mounted on the beamline.
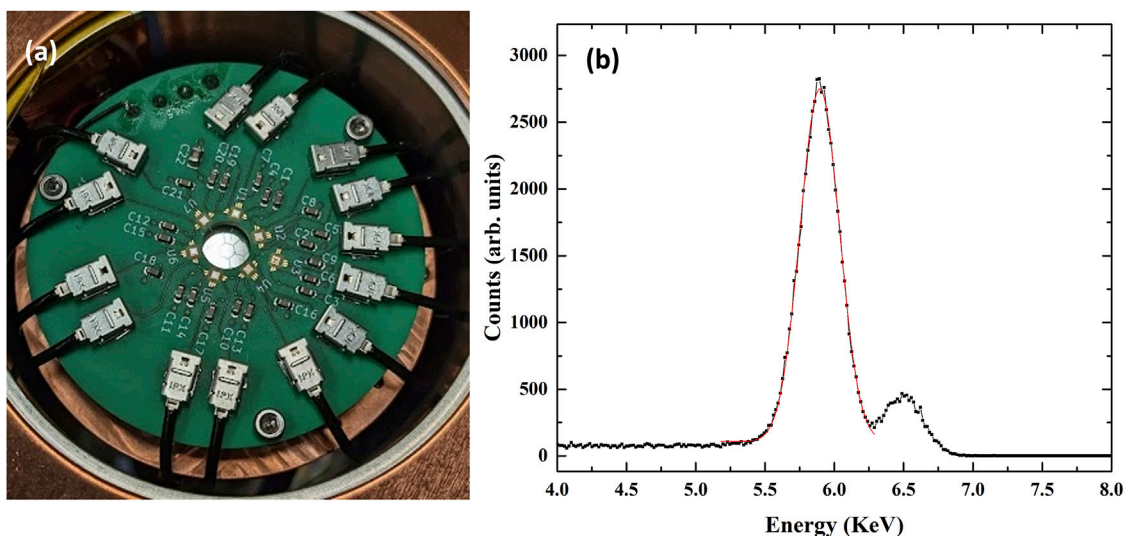

FIGURE 10
(a) Sensor wire bonded to Cube preamplifier. **(b)** Response of ^{55}Fe emission lines.

Geronimo et al., 2010). Sensors with integrated FETs rely on conventional contact lithography to create the necessary microstructures, which limit the achievable feature sizes. As a result, these transistors tend to be large and exhibit suboptimal electrical properties. Advancements in commercial complementary metal-oxide-semiconductor (CMOS) technology have significantly improved scaling and speed, enabling the fabrication of sub-micron structures in commercial foundries. By decoupling the preamplifier from the sensor, commercial CMOS processes can be leveraged for front-end FETs. While this approach introduces additional capacitance from the sensor-FET connection, it is outweighed by the substantial increase in the input FET's transconductance. One example of a low-noise CMOS preamplifier using this approach is the "CUBE", developed by Politecnico di Milano and XGLab (Bombelli et al., 2011). The CUBE operates in a pulse-reset mode, where a MOS transistor periodically resets the charge accumulated in the feedback capacitor, ensuring stable and efficient operation. BNL has fabricated a 7-channel hexagonal 1.7 mm array Ge sensor (Gepta-EX) read out by a CUBE preamplifier for XAFS applications. A Ge based spectroscopy detector would enhance data

quality especially for all 4D elements. This would open interesting areas of science, including catalysis, photovoltaic and energy storage materials, nuclear waste management and nuclear engineering materials, surface coatings, computer memory applications, etc. Figure 10a shows the seven channel Ge detector connected to the CUBE pre-amplifier and Figure 10b shows the detector response for 55Fe radioactive source. The measured energy resolution is about 254 eV.

Although high-quality detector-grade materials have enabled the development of efficient Ge-based detectors with reasonable depletion voltages and excellent charge collection efficiencies, their full potential remains limited by the lack of reliable, thin hole-blocking (n$^+$) contacts. Complex device geometries, such as drift sensors, which are feasible in Si-based devices, are not yet achievable in Ge due to the difficulty of precisely separating hole-blocking layers from electron-blocking (p$^+$) contacts on the same side of the device (Gatti and Rehak, 1984). Thin electron-blocking contacts can be readily formed by depositing metals like Au, Ni, or Cr on Ge or by creating a thin B-doped p$^+$ layer (Protic and Riepe, 1985; Protic et al., 2005; Malm, 1975). However, traditional hole-blocking contacts rely
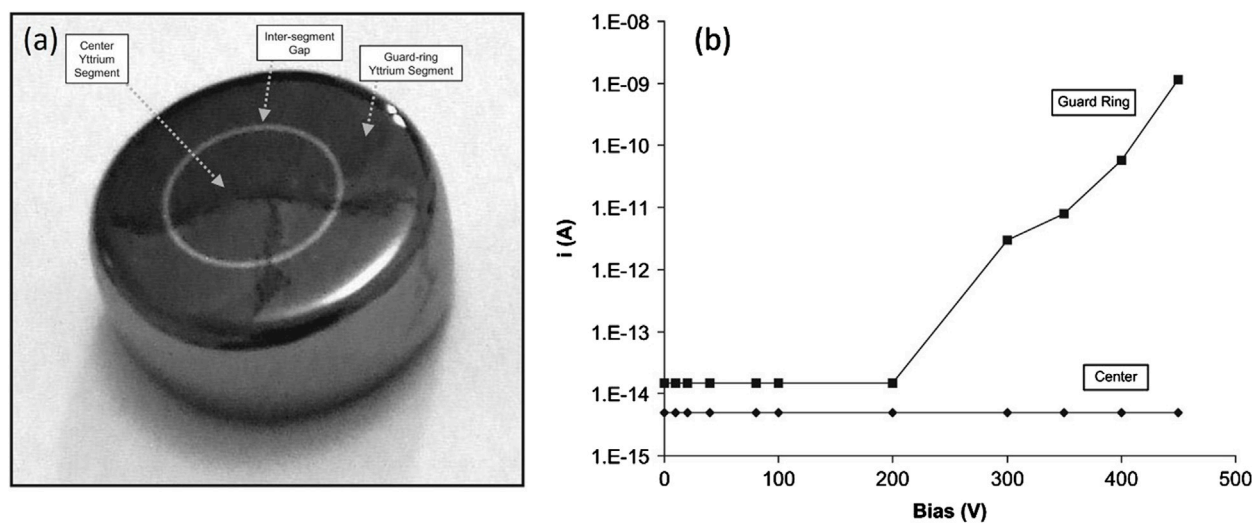
FIGURE 11
(a) Photograph of a segmented high-purity germanium semiconductor detector. The visible segmented contact is a thin (~1,000 Å) layer of yttrium. The yttrium contact is segmented into a center and guard-ring segment through the use of photolithography. **(b)** Leakage current as a function of bias voltage from an example detector at 80 K. Figures from (Hull et al., 2011).

on thick Li-diffused layers, which can be hundreds of micrometers thick, making lithography and segmentation challenging. The development of a robust, thin hole-blocking contact for Ge has been an ongoing challenge. While phosphorus-implanted n$^+$ contacts are a natural solution, their implementation in Ge is difficult due to the high-temperature annealing required for activation, which can degrade the crystal's charge collection properties. Recent efforts have focused on amorphous silicon and germanium contacts as reliable alternatives (Hansen, 1971; Amman et al., 2007). The amorphous germanium contacts act as a Schottky metal-semiconductor contacts creating electron and hole barrier equal to half the band gap of Ge. As a result, it effectively blocks both charge carriers and maintains low leakage current under either bias condition. Recently, yttrium-based (a low work function metal) thin hole blocking contact on Ge was fabricated in the laboratory of PHDs Co. in Oak Ridge, TN (Hull et al., 2011). It was reported that sputtered yttrium metal for a thin hole blocking contact on both p$^-$ and n$^-$ type germanium. Sputter deposition enables easy segmentation of the contact and offers practical fabrication advantages. The detector leakage-current behavior shows strong rectification of the yttrium contact on p-type germanium. Figure 11 shows a photograph of segmented high-purity germanium detectors with yttrium contact and the leakage current as a function of applied voltage for a detector at 80 K. Interestingly, although yttrium, with a work function of 3.1 eV, functioned effectively as a hole-blocking contact, samarium, which has an even lower work function of 2.7 eV, did not. This highlights the significant role of interface states in determining the barrier height of metal-semiconductor interfaces (Rumaiz et al., 2023).

3.1 Considerations

Germanium (Ge) detectors remain essential for high-resolution radiation detection, particularly in X-ray and gamma-ray

spectroscopy. While significant progress has been made in developing Ge-based detectors for hard X-ray and gamma-ray applications using trench segmentation, Li-diffused, and amorphous semiconductor contacts, several challenges still need to be addressed to fully realize their potential. Two critical areas for improvement are the development of a stable field oxide to enable large-scale pixelation and the advancement of traditional phosphorus-based n-type contacts. The hygroscopic nature of native Ge oxide has been a longstanding issue, but recent studies on capping layers using ALD-grown Al_2O_3 have shown promising results (Aso et al., 2025). Similarly, alternative surface annealing techniques, such as laser or microwave annealing, offer potential solutions for phosphorus activation while preserving the crystal's charge collection efficiency.

4 Amorphous selenium detectors for high spatial resolution imaging

Amorphous selenium (a-Se) is wide bandgap (~2.1 eV) semiconductor which possesses unique properties that make it an excellent candidate for radiation detection (Kasap et al., 2009). Discovered as an X-ray photoconductor in the 1940s, a-Se was widely used in photocopiers until being replaced by organic photoconductors. As a direct detection semiconductor with a low melting point, it allows for the deposition of thick, uniform layers over large areas at low temperatures through thermal evaporation, simplifying and reducing the cost of production. This enabled its integration with large area thin-film transistors (TFTs) for X-ray imaging applications. a-Se detectors exhibit low dark current, typically around 10 pA/mm^2 under moderate electric fields, minimizing noise and ensuring high image quality (Schein, 1974). Functioning as a p-type semiconductor, a-Se has hole mobility significantly higher than electron mobility, with the μτ product (mobility-lifetime product) for holes being an order of magnitude
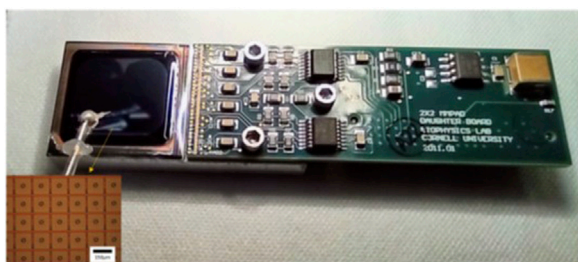
FIGURE 12
MM-PAD ASIC with a-Se mounted on the daughter board. Inset shows the pixel array with top metal pads extended for improved fill factor.

greater than that of electrons. The addition of impurities such as chlorine further enhances this property, improving charge transport efficiency (Kolomiets and Lyubin, 1973).

The primary advantage for using amorphous selenium (a-Se) lies in its ability to be directly deposited onto readout electronics, enabling monolithic integration. Additionally, a-Se offers inherently high spatial resolution, making it well suited for imaging platforms with pixel sizes below 10 μm. Achieving such fine resolution is challenging with conventional hybrid bonding techniques, where pixel pitch is limited by the physical constraints of the bump bonding process. Its high atomic number reduces susceptibility to X-ray Compton scattering, making it particularly effective for imaging at energies above 60 keV. One of its most significant attributes is its ability to withstand high voltage biases—typically around 70 V/μm allowing for impact ionization and avalanche multiplication, further enhancing its detection capabilities (Juška and Arlauskas, 1980). Current state-of-the-art commercial a-Se medical imaging detectors typically utilize thin-film transistor (TFT) arrays (Zhao and Rowlands, 1995). However, advancements in CMOS technology offer new possibilities. CMOS arrays enable much smaller pixel sizes and provide capabilities for charge integration and photon counting, which are crucial for improving detection efficiency and resolution. The low deposition temperatures required for a-Se allow it to be deposited directly on CMOS a readout ASICs without damaging the underlying circuitry, simplifying the fabrication process and reducing costs. The detector group at BNL with collaborators from Cornell University and Stony Brook University fabricated X-ray detectors by direct deposition of a-Se on a Mixed-Mode Pixel Array (MM-PAD) CMOS application specific circuit (Han et al., 2023). The details of the readout chip can be found in previous works (Philipp et al., 2016, 2020). Briefly, the MM-PAD ASIC is a high dynamic range hybrid pixel array detector designed for kilohertz imaging of hard X-rays. This ASIC integrates both analog and digital signal processing components within each pixel, optimizing it for high-speed and high-flux X-ray applications. Figure 12 shows the MM-PAD ASIC with a-Se deposition and chromium top metal electrode.

The dynamic response of a-Se detector was measured by quick exposure of a knife edge. Figure 13 displays the decay of the detector's response over time, starting 100 ms before the shutter closes and continuing until 2,400 ms after the shutter closes. Each frame captures the state of the detector at specific intervals, providing a detailed view of its temporal response. At −100 ms (before the shutter closes), the detector is fully illuminated, showing

a high and uniform response; at 0 ms (the moment the shutter closes), there is an immediate drop in intensity. Between 100 ms and 2,400 ms, the images reveal a gradual signal decay—initially rapid, then slowing over time—suggesting the progressive release of trapped charges from shallow traps (Zhao and Zhao, 2008).

While the temporal response of a-Se exhibits signal decay over several seconds, it provides exceptional spatial resolution. The detector's spatial resolution is typically evaluated using the edge spread function (ESF), which characterizes its response to a step change in X-ray intensity across a sharp edge. For the a-Se detector, this was measured by positioning a tantalum knife edge at a slight angle relative to the detector. This configuration enables sub-pixel sampling of the ESF within a single image. The resulting point spread function (PSF) for Cu Kα radiation was approximately 5 μm, closely matching Monte Carlo-Boltzmann Transport Equation simulations, which predicted a PSF of 2.4 μm (Han et al., 2023). a-Se addresses pixel size limitation of bump bonds in hybrid X-ray detectors especially for hard X-ray detection. Imaging for X-rays with one megapixel detector with a-Se coupled to a CMOS active pixel sensor (APS) with a pixel pitch of 7.8 μm has been designed, fabricated, and commercially available (Scott et al., 2021).

a-Se undergoes impact ionization at voltages over 70 V/μm and was first reported in 1980 (Zhao and Rowlands, 1995). The first commercial application of avalanche photomultiplication was shown with the development of High-gain Avalanche Rushing Photoconductor (HARP) (Tanioka et al., 1987). This was integrated into commercial TV pick-up tubes. The incident light from the object is first absorbed in the a-Se layer. Under strong electric field the drifting holes undergoes impact ionization giving an effective quantum efficiency of greater than one. Due to the low mobility-lifetime product of electrons they are quickly neutralized. The extent of this avalanche multiplication and consequently the effective quantum efficiency which depends on both the applied field strength and the thickness of the photoconductor. It must be noted that even though the phenomenon of avalanche multiplication has been known for about four decades, the nature of impact ionization is still an ongoing scientific problem (Rubel et al., 2004; Kasap et al., 2004; Mukherjee et al., 2023).

4.1 Considerations

The a-Se detector exhibits high spatial resolution and its low-temperature deposition technique eliminates the need for hybrid bonding by enabling direct deposition. When integrated with advanced pixel sensor readout, it provides a robust platform for high-resolution imaging. However, its dynamic response reveals a signal decay over several seconds. While this limits its suitability for time-resolved measurements, the detector's exceptional spatial resolution at high energies makes it valuable for applications where time resolution is determined by the X-ray duration, such as single-shot radiography.

5 Cesium lead bromide as X-ray and gamma-ray detector

The interest in realizing hard X-ray and gamma detectors that can be operated at room temperature while providing performances
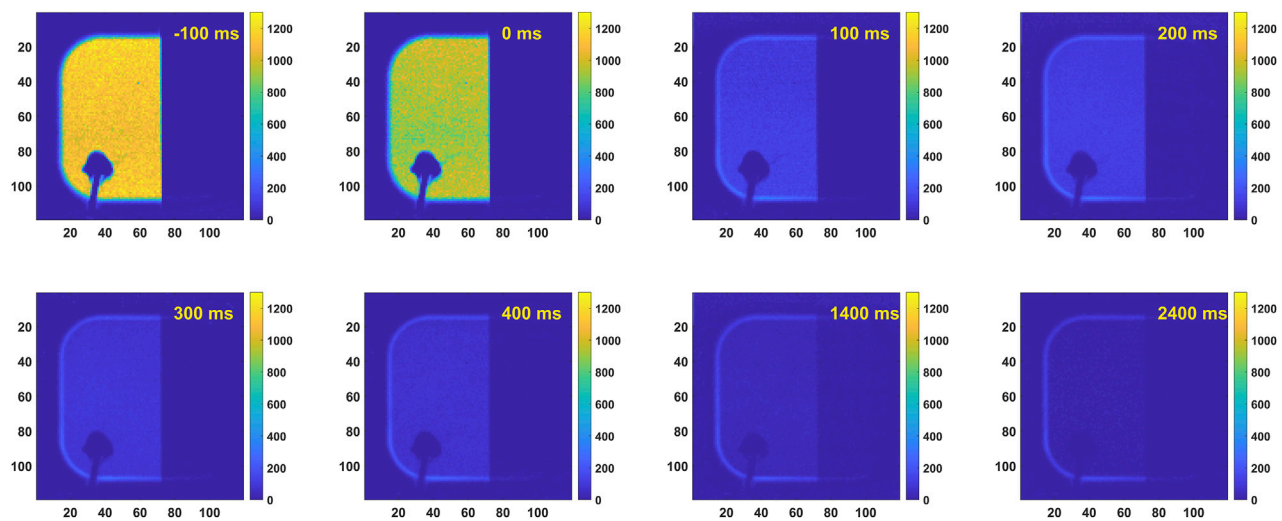
FIGURE 13
Extinction lag in the a-Se response via successive detector frames as the shutter transitions from the "on" to the "off" state, with the response being recorded from 100 ms prior to the shutter closure until 2,400 ms after the shutter closure. Figure from (Han et al., 2023).

comparable to those of Ge or CZT has attracted interest in the development of high-Z semiconductor material with larger band gaps to minimize the noise and dark currents arising from thermally activated carriers. Within the realm of these large band-gap materials the inorganic perovskites belonging to the alkali lead halide family have been demonstrating in the last year performances that are approaching those of state-of-the-art high-Z semiconductors triggering numerous studies aimed at developing techniques for their synthesis on a large scale that can allow the realization of compact advanced X-ray and gamma detectors with reduced cost for manufacturing and operation. Within the family of alkali lead halides (chemical formula $CsPbA_3$ with A = I, Cl, Br), the $CsPbBr_3$ appears one of the most studied material. With a direct band gap of about 2.3 eV a high mass density (4.85 g/cm^3) and an attenuation coefficient comparable to CZT this semiconducting material has been identified as one of the most promising candidates for the detection of hard X-rays and gamma-rays. It has been demonstrated that it is possible to fabricate detectors from pure high-quality crystals that can operate with low dark current at room temperature. In addition, $CsPbBr_3$ material has high mobility-lifetime products (μτ) for both electrons and holes, which are already on the order of 10^{-3} cm^2/V. These properties are fundamental for high charge collection efficiency. Although the reproducibility of the performances still represents a challenge as it often depends on the synthesis process and conditions used to grow the CsPbBr3 crystal, this material has shown promising results yielding 1.4% energy resolution for 662 keV gamma rays (He et al., 2021) and radiation hardness up to gamma ray doses up to 1 Mrad where the energy resolution and μτ showed negligible changes after irradiation (De Siena et al., 2023). The uniformity of the response is generally affected by structural and compositional homogeneity, since there are different stable phases with different stoichiometry and by the presence of defects that can trap carriers (Zhang et al., 2018).
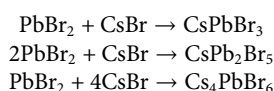
5.1 CsPbBr$_3$ challenges for charge collection detectors

Critical to increase the performance of the material for the charge collection is the availability growth techniques that can produce large crystals with reduced defect densities achieving high values for bulk resistivity $10^8 \, \Omega \cdot$cm, carrier mobility, and stability of their performance during operation. Between the room temperature and the melting point of the $CsPbBr_3$ (the latter being measured in the range of 567 °C–591 °C (Kanak et al., 2022) the crystal structure undergoes two phase transitions. As the temperature rises structural transition from orthorhombic to tetragonal happens at about 88 °C and then to cubic at 130 °C (Stoumpos et al., 2013). When such phase transitions occur, the lattice structure is distorted and mechanical stress originates inside the crystal, which may lead to the formation of defects that will affect the material properties relevant for application in radiation detection. The presence of impurities in the precursors used for the synthesis of the crystal will affect the defect and trap densities, affecting the carriers' transport and the performance of the detector. Mitigation strategies in crystal synthesis often include additional process steps aimed at purifying the reagents used before the crystal is grown (Chung et al., 2024). Furthermore, there are other stable stochiometric compounds that are rich in Cs or Pb (such as $CsPbBr_5$ and Cs_4PbBr_6), which complicate the scenario calling for further improving the control of the growth process to minimize the presence of other phases (Zhang et al., 2018). $CsPbBr_3$ crystals are known to suffer from ion migration (Zhang et al., 2020a), a process initiated by intrinsic defects formed during crystal growth. This can lead to increased defect densities and a subsequent degradation of carrier transport properties. Encouragingly, recent studies have shown that the polarization effects caused by ion migration can be significantly mitigated by carefully selecting the crystal orientation along which the voltage is applied. This approach

helps preserve both high energy resolution and long-term stability in sensor operation (Toufanian et al., 2022).

5.2 CsPbBr₃ crystal growth methods

Several methods have been used to successfully synthesize CsPbBr₃. Some of them like Inverse Temperature Crystallization (ITC) and the Anti-solvent Vapor-assisted Crystallization (AVC) are simple liquid solution methods carried at relatively low temperatures that can produce crystals with lateral sizes up to few millimeters. The Bridgman method and the Electronic Dynamic Gradient (EDG), on the other hand, require reaching the melting temperature of the CsPbBr₃ powders at about 600 °C and can produce much larger crystal ingots with sizes up to 65 mm in diameter and several centimeters in length (Toufanian et al., 2022). The CsPbBr₃ powders used for Bridgman or EDG can be produced using the chemical reaction between two PbBr₂ and CsBr solutions in aqueous solution of hydrobromic acid (HBr). Depending on reactants' concentrations in the solutions and on their molar ratio the following reactions can take place, each yielding different stochiometric stable compounds:

$$PbBr_2 + CsBr \rightarrow CsPbBr_3$$
$$2PbBr_2 + CsBr \rightarrow CsPb_2Br_5$$
$$PbBr_2 + 4CsBr \rightarrow Cs_4PbBr_6$$

Detailed studies have identified the optimal molar concentration for the reactant of 1.9 mol/L for PbBr₂ and 1.1 mol/L for CsBr and with the molar ratio PbBr₂ to CsBr of 1.01:1 as reported in (Zhang et al., 2018). An alternative method to produce the CsPbBr₃ stochiometric powder sees the use of Cs₂CO and PbO solution in HBr with an optimized molar ratio of 1.25:1 of Cs₂CO to PbO (Kunar et al., 2023). Purification of precursors achieved either by sublimation of the PbBr₂ and CsBr precursors or by frit filtering the melted CsPbBr₃ powders is critical to remove impurities and obtain single crystal with improved performance in terms of higher bulk resistivity, carrier mobilities and lifetimes yielding increased energy resolution for the detection of hard X-ray (Chung et al., 2024). The bulk resistivity of CsPbBr₃ high quality single crystals obtained from high quality precursors grown with either Bridgman or EDG methods was measured to be in the range of $10^9–10^{10}$ Ω cm (Chung et al., 2024; Zhang et al., 2018). These values are comparable to the ones achieved in bulk CZT or TlBr (Li et al., 2024; Datta et al., 2018) which, on the other hand, have typically one order of magnitude lower impurities concentrations highlighting the resilience of CsPbBr₃ with respect to crystal defects.

Depending on the application, if the size of the crystals can be limited to lateral size of few millimeters, the growth from liquid solution either by ITC or AVC may represents a valid alternative to Bridgeman or EDG methods. The ITC method leverages the decreasing material's solubility as the temperature of the solution increases. Typically, CsBr and PbBr₂ are dissolved in Dimethylsulfoxide (DMSO) with molar ratio between PbBr₂ and CsBr at ~2:1 to obtain the pure CsPbBr₃ phase. Deviations from this molar ratio will result in precipitates that are either rich in Pb or Cs content (Dirin et al., 2016). In ITC growth the sharp decrease of

CsPbBr₃ solubility in DSMO happen in the range of 75–90 °C. The range of temperatures for this solubility drop can be widened to 25–110 °C with the addition of a cyclohexanol (CyOH) and dimethylformamide (DMF) mixture to the precursor solution. The smoother decrease in solubility with temperature results in a slower over-saturation transition compared to the solution based on DMSO alone resulting in a decrease in the number of nucleation sites, producing a lower number of crystals growing with larger overall sizes (Dirin et al., 2016). The growth of CsPbBr₃ crystal in ITC occurs preferentially along the (002) crystal direction because the adhesion energy to the crystal facets related to this crystal direction are larger then in other facets. This effect results in the growth of crystals presenting an elongated bar shape. The addition of choline bromide (CB) in the precursor solution is shown to be effective in mitigating this effect, resulting in the growth of cubic-shaped crystals with also drastically reduced defect densities (Feng et al., 2020). The growth with ITC method usually yields small crystals, only a few millimeters per side, but the use of a small seed resulted in larger crystals sizes, up to 10 mm per side (Zhang et al., 2020b). A modified ITC method make use of a 48% HBr and water mixture as solvent instead of DMSO (Peng et al., 2021). In this case, the solubility of CsPbBr₃ decreases as the solution temperature decreases. The temperature of the solution is lowered from about 100 °C to 25 °C with a rate of about 2 °C/h. A seed is used to enable the formation of larger crystals. The crystal grown in water have shown improved performance (shorter photoluminescence decay time, improved carrier mobility, and X-ray sensitivities larger then 4,086 μC Gy$_{air}^{-1}$ cm^{-2}) if compared to similar ones grown in DMSO. The AVC method leverages the different solubility of CsPbBr₃ in different solvents. Two solvents are required for the growth: one showing large and the other a poor solubility for CsPbBr₃ with both solvents being also mutually soluble. The precursors are initially prepared with the solvent with the large solubility for CsPbBr₃, then the poor solubility solvent is slowly allowed to diffuse into the solution by vapor phase. As the two solvents get mixed the solution becomes more and more supersaturated and the crystals begin to nucleate and grow. DMSO and methanol have been used as solvents with respectively large and poor solubility to grow CsPbBr₃ crystals (Rakita et al., 2016). Similarly to the ITC growth process the AVC methods require a careful optimization of the concentrations of precursors to improve the quality and increase the size of the crystal samples (Rakita et al., 2016). Figure 14 shows the some of the characteristics orange colored CsPbBr₃ crystal growth at BNL using the ITC method and the fluorescence light emitted once under UV ligth exposure.

5.3 CsPbBr₃ performance

The performance of sensors made from single-crystal CsPbBr₃ largely depends on key parameters such as the samples' electrical resistivity, the lifetime and mobility of electrons and holes, response stability over time, energy resolution, and radiation dose sensitivity. The highest reported resistivity for a single crystal is ~343 GΩ ·cm was achieved with a sample grown using the Bridgman method (Stoumpos et al., 2013). Other growth techniques have also produced samples with resistivity in the GΩ range,
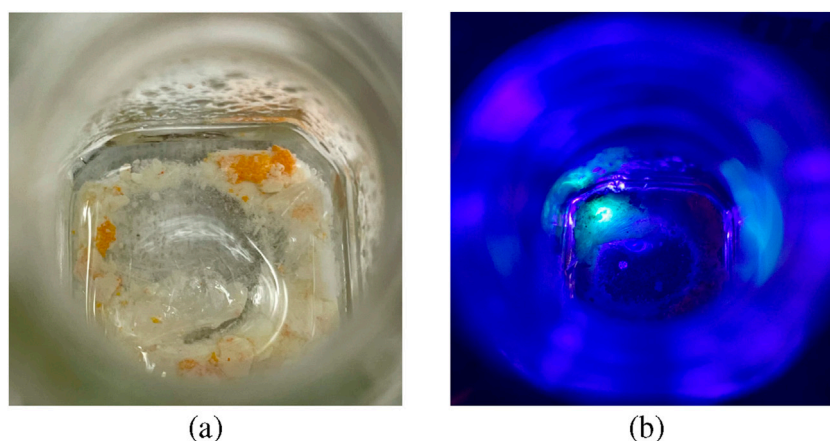
FIGURE 14
CsPbBr$_3$ **(a)** Crystals growth at BNL with visible orange grain dimensions of ~ 2 mm × 2 mm **(b)** Green photoluminescnce emitted under 405 nm UV laser excitation. The luminescence is localized to the upper-left region, where the focused laser beam ~2 mm beam waist) was directed through the glass onto the crystal. Other orange crystals were not illuminated during this image, but similar photoluminescence was observed at different positions and on additional crystals from the same batch when excited under identical conditions.

sufficient for the development of sensors operating in charge-collection mode (Stoumpos et al., 2013; Wang et al., 2022). Differences in impurity concentrations, characteristic of various growth methods, primarily influence carrier mobility and lifetime by affecting the density of recombination centers and traps within the bulk. As a result, reported carrier lifetimes for both electrons and holes vary widely, spanning more than two orders of magnitude—from 2.5 ms to over 800 ms (Qin et al., 2025; He et al., 2021; Stoumpos et al., 2013; He et al., 2019; Zhang P. et al., 2020; He et al., 2018). Carrier mobilities in CsPbBr$_3$ have been reported in the range between 20 and 500 cm^{2}V^{-1}s^{-1} (Qin et al., 2025; He et al., 2021; Stoumpos et al., 2013; Wang et al., 2022; He et al., 2019; Zhang et al., 2022; Pan et al., 2020; Zhang P. et al., 2020, 2017; Peng et al., 2021; Feng et al., 2020). Other High-Z semiconductors used or being developed for gamma or X-ray like HPGe and CZT have much higher carrier mobilities than CsPbBr$_3$ already at room temperature. HPGe has shown carrier mobilities at room temperatures of about 1,000 cm^{2}V^{-1}s^{-1} that increased to more than 40,000 cm^{2}V^{-1}s^{-1} when samples are cooled to 77 K (Palleti et al., 2024). CZT crystals have mobilities in the range of 1,000 cm^{2}V^{-1}s^{-1} at room temperature (Wu et al., 2022). Finally, a-Se and TlBr have much shorter carrier mobilities of about 2.6 cm^{2}V^{-1}s^{-1} (Kabir and Hijazi, 2014) and 23 cm^{2}V^{-1}s^{-1} (Watanabe et al., 2024) respectively. Margins may still exist to further increase mobility of CsPbBr$_3$ above the 500 cm^{2}V^{-1}s^{-1} value (Stoumpos et al., 2013). Although the largest values have been obtained for crystals grown using Bridgman method other techniques based on liquid solution have yielded mobilities well above the 100 cm^{2}V^{-1}s^{-1} (Zhang et al., 2017; Peng et al., 2021; Feng et al., 2020) indicating the possibility to further improve carrier transport performances especially for application where high repetition rates of signals are expected. The resulting figures of merit for carrier transport, expressed as μτproducts, have been reported to span several orders of magnitude—from 8.5×10^{-5} to 2.5×10^{-2} cm^2 V^{-1} (Qin et al., 2025; He et al., 2021; Stoumpos et al., 2013; Wang et al., 2022). CsPbBr^3 single crystals grown via the Bridgman or ITC methods have been successfully used to fabricate gamma-ray detectors, achieving energy resolutions well below 10% for 662 keV photons at room temperature (Qin et al., 2025; Pan et al., 2020; Zhang et al., 2023), with an outstanding resolution of 1.4% reported in (He et al., 2021).

X-ray sensitivity often varies between individual samples due to differences in carrier transport properties, as well as external factors such as X-ray dose, energy, and the applied bias voltage. Nonetheless, sensitivities exceeding 8,000 μC Gy$_{air}^{-1}$ cm^{-2} have been achieved, with detectable dose rates as low as 0.02 Gy$_{air}^{-1}$ s^{-1} (He et al., 2022). The considerable variation in the performance of CsPbBr^3-based detectors has been primarily attributed to differences in material composition and crystal structure resulting from the specific growth methods employed. Notably, introducing a small amount of Rb doping (0.037%) into Cs$_{1-x}$Rb$_x$PbBr$_3$ single crystals has been shown to enhance the μτ product for holes in solution-grown samples, reaching values as high as 7.2×10^{-4} cm^{2}V^{-1}. This Rb doping also significantly improves the X-ray sensitivity of single-crystal detectors, achieving up to 8,097 μC Gy$_{air}^{-1}$ cm^{-2}. The improvement is attributed to a marked reduction in trap density, increased electrical resistance, and enhanced charge carrier mobilities (Li et al., 2020).

5.4 Testing a CsPbBr$_3$ detector

The spectroscopic performance to gamma-ray of a bar-shaped CsPbBr$_3$ 3 × 3 × 6 mm^3 detector was evaluated using the VFG configuration, as described in Section 2.1. The detector under test consisted of a 3 × 3 × 6 mm^3 CsPbBr$_3$ crystal, grown and fabricated by RMD. Measurements were carried out using our standard characterization setup which is routinely employed for testing CZT and TlBr detectors at BNL (Kargar et al., 2022).

Figure 15 presents the measured energy spectra before and after correction, including the raw, 1D, and 3D corrected data.
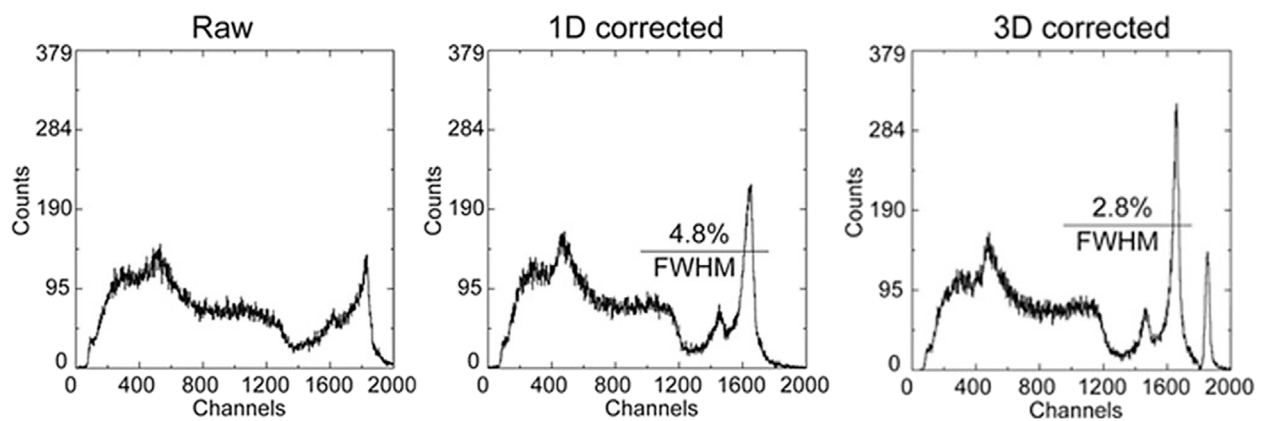
FIGURE 15
Exemplary CsPbBr$_3$ detector response in a VFG configuration showing the raw, 1D, and 3D corrected measured spectrum for $3 \times 3 \times 6$ mm^3 device under irradiation of an uncollimated ^{137}Cs radioactive source.

(a)   (b)
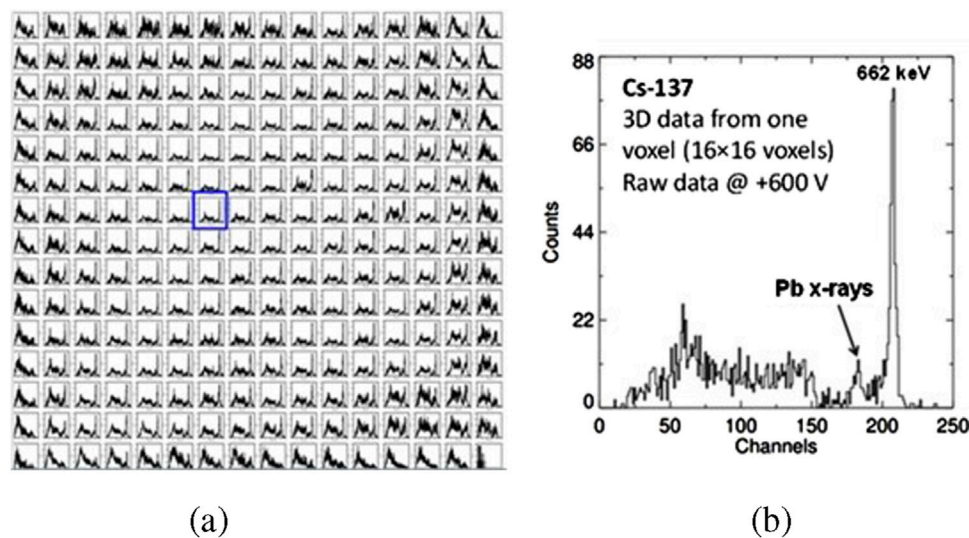
FIGURE 16
(a) Array of 32 × 32 for ^{137}Cs spectra associated with the XY location in the 3.1 mm × 3.1 mm area of the detector. (b) Magnified ^{137}Cs pulse height spectrum for one of the best voxels marked inside a blue box in (a).

The energy resolution is quantified in terms of FWHM with values indicated in the figure for both the 1D and 3D corrected cases, demonstrating significant improvement in spectral performance through advanced correction techniques. To visualize the spatial non-uniformity of the detector response, Figure 16a displays an array of 32×32 individual 137Cs spectrum, each corresponding to a specific XY voxel within the central 3.1 mm × 3.1 mm region of the crystal's surface. This visualization highlights variations in spectral quality across the detector face. For comparison, Figure 16b shows a magnified pulse height spectrum from one of the best-performing voxels, as marked by a blue box in Figure 16a. The high-quality photopeak observed in this voxel underscores the intrinsic potential of CsPbBr$_3$ for gamma-ray spectroscopy when paired with voxel-wise correction.

5.5 Considerations

CsPbBr$_3$ represents possibly the most studied and promising inorganic High-Z perovskite material for the detection of gamma and X-ray photons. The experimental efforts in the last decade have demonstrated the realization of detectors whose performances are closely approaching the ones of other well-known materials like Ge or CZT. While the perovskite structure appears to be more tolerant to defects respect to other materials, some operational aspects related to the short and long term stability related to the ion migration still need to be properly addressed. Several pathways for the synthesis of high-quality materials have been identified, but there are still large variations on the physical parameters relevant for detector operation. This highlights the need of continued efforts to further improve the reliable realization of crystals with reproducible

properties that will allow their use to transition from research to applications.

6 Conclusion

In recent years, the exploration of new semiconductor materials and architectures has expanded the capabilities of radiation detectors beyond traditional silicon. Materials such as germanium (Ge), cadmium-telluride (CdTe)/cadmium-zinc-telluride (CZT), thallium bromide (TlBr), amorphous selenium (a-Se) and halide perovskites (e.g., $CsPbBr_3$) have garnered significant attention due to their favorable properties for X-ray and gamma-ray detection. These materials offer higher atomic numbers and densities compared to silicon, which improves photon stopping power and consequently detection efficiency for higher energy photons. Additionally, some of these materials allow for room-temperature operation, eliminating the need for cryogenic cooling and simplifying system integration.

Hybrid detector technologies, which combine semiconductor sensors with custom-designed readout electronics through bump bonding or direct integration, have further enhanced detector performance. These systems enable the separation and optimization of the sensor and electronics layers. For instance, a high-Z semiconductor layer can be bonded to a high-speed CMOS readout chip, merging excellent detection efficiency with fast and low-noise signal processing. This flexibility has led to the development of photon-counting detectors with energy discrimination capabilities for high-energy X-rays, making them invaluable tools in synchrotron science, medical imaging, and security screening.

In parallel, new readout ASICs have made remarkable progress in achieving lower noise, reduced power consumption, and higher frame rates. These innovations support a growing demand for compact, low-mass detectors in space instrumentation and high-energy physics experiments where material budget and timing resolution are critical. Applications of semiconductor radiation detectors are now more diverse than ever. In medicine, CdTe and CZT-based detectors are used in digital radiography, computed tomography, and positron emission tomography. In synchrotron and free-electron laser facilities, detectors with high dynamic range and fast readout are essential for time-resolved and high-throughput experiments, including X-ray diffraction, spectroscopy, and imaging. In homeland security, rugged and compact detectors based on wide-bandgap materials are deployed in portable systems for radioactive material identification and screening.

Looking forward, the next-generation of semiconductor radiation detectors will likely be driven by advances in material science, nanofabrication, and AI-assisted data processing. Better crystal growth techniques combined with engineered heterostructures and advances in materials processing could lead to the development of better detectors especially for high-energy X-ray needs. Concurrently, developments in integrated circuit design will continue to push the limits of readout speed, resolution, and in-pixel processing. Ultimately, the synergy between semiconductor technology and radiation detection continues to evolve, enabling ever more sophisticated systems that are smaller, faster, and more capable, meeting the growing demands of scientific discovery, medical diagnostics, security, and environmental monitoring.

Author contributions

Funding

Acknowledgments

Conflict of interest

The authors declare that the research was conducted in the absence of any commercial or financial relationships that could be construed as a potential conflict of interest.

Generative AI statement

The author(s) declare that no Generative AI was used in the creation of this manuscript.

Any alternative text (alt text) provided alongside figures in this article has been generated by Frontiers with the support of artificial intelligence and reasonable efforts have been made to ensure accuracy, including review by the authors wherever possible. If you identify any issues, please contact us.

Publisher's note

All claims expressed in this article are solely those of the authors and do not necessarily represent those of their affiliated organizations, or those of the publisher, the editors and the reviewers. Any product that may be evaluated in this article, or claim that may be made by its manufacturer, is not guaranteed or endorsed by the publisher.

References

Abdesselam, A., Akimoto, T., Allport, P., Alonso, J., Anderson, B., Andricek, L., et al. (2006). The barrel modules of the atlas semiconductor tracker. *Nucl. Instrum. Methods Phys. Res. Sect. A Accel. Spectrom. Detect. Assoc. Equip.* 568, 642–671. doi:10.1016/j.nima.2006.08.036

Amman, M., Luke, P., and Boggs, S. (2007). Amorphous-semiconductor-contact germanium-based detectors for gamma-ray imaging and spectroscopy. *Nucl. Instrum. Methods Phys. Res. Sect. A Accel. Spectrom. Detect. Assoc. Equip.* 579, 886–890. doi:10.1016/j.nima.2007.05.307

Aso, T., Kuwazuru, H., Wang, D., and Yamamoto, K. (2025). Al2o3 growth on ge by low-temperature (~90 c) atomic layer deposition and its application for mos devices. *Mater. Sci. Semicond. Process.* 190, 109372. doi:10.1016/j.mssp.2025.109372

Bertuccio, G., and Caccia, S. (2007). Progress in ultra-low-noise asics for radiation detectors. *Nucl. Instrum. Methods Phys. Res. Sect. A Accel. Spectrom. Detect. Assoc. Equip.* 579, 243–246. doi:10.1016/j.nima.2007.04.042

Bolotnikov, A., Camarda, G., Carini, G., Fiederle, M., Li, L., McGregor, D., et al. (2006). Performance characteristics of frisch-ring cdznte detectors. *IEEE Trans. Nucl. Sci.* 53, 607–614. doi:10.1109/TNS.2006.871509

Bolotnikov, A., Camarda, G., Geronimo, G. D., Fried, J., Hodges, D., Hossain, A., et al. (2020). A 4 × 4 array module of position-sensitive virtual frisch-grid cdznte detectors for gamma-ray imaging spectrometers. *Nucl. Instrum. Methods Phys. Res. Sect. A Accel. Spectrom. Detect. Assoc. Equip.* 954, 161036. doi:10.1016/j.nima.2018.07.090

Bolotnikov, A., Carini, G., Chekhlov, M., Dellapenna, A., Fried, J., Haupt, J., et al. (2022). Radiation effects induced by the energetic protons in 8x8x32 mm3 cdznte detectors. *Nucl. Instrum. Methods Phys. Res. Sect. A Accel. Spectrom. Detect. Assoc. Equip.* 1039, 166927. doi:10.1016/j.nima.2022.166927

Bolotnikov, A., Carini, G., Dellapenna, A., Deptuch, G., Fried, J., Herrmann, S., et al. (2024). 3x3 array module of 8 × 8 × 32 mm3 position-sensitive virtual frisch-grid cdznte detectors for imaging and spectroscopy of cosmic gamma-rays. *Nucl. Instrum. Methods Phys. Res. Sect. A Accel. Spectrom. Detect. Assoc. Equip.* 1064, 169328. doi:10.1016/j.nima.2024.169328

Bombelli, L., Fiorini, C., Frizzi, T., Alberti, R., and Longoni, A. (2011). ""cube", a low-noise cmos preamplifier as alternative to jfet front-end for high-count rate spectroscopy," in *2011 IEEE nuclear science symposium conference record*, 1972–1975. doi:10.1109/NSSMIC.2011.6154396

Bunemann, O., Cranshaw, T. E., and Harvey, J. A. (1949). Design of grid ionization chambers. *Can. J. Res.* 27a, 191–206. doi:10.1139/cjr49a-019

Chung, D. Y., Lin, W., Unal, M., Phan, Q. V., Pandey, I. R., Vitt, R., et al. (2024). Growth of high-purity cspbbr3 crystals for enhanced gamma-ray detection. *Cryst. Growth & Des.* 24, 9590–9600. doi:10.1021/acs.cgd.4c01109

Churilov, A. V., Ciampi, G., Kim, H., Higgins, W. M., Cirignano, L. J., Olschner, F., et al. (2010). TlBr and TlBr I1− crystals for γ-ray detectors. *J. Cryst. Growth* 312, 1221–1227. doi:10.1016/j.jcrysgro.2009.10.055

Datta, A., Becla, P., Guguschev, C., and Motakef, S. (2018). Advanced crystal growth techniques for thallium bromide semiconductor radiation detectors. *J. Cryst. Growth* 483, 211–215. doi:10.1016/j.jcrysgro.2017.12.008

De Geronimo, G., Rehak, P., Ackley, K., Carini, G., Chen, W., Fried, J., et al. (2010). Asic for sdd-based x-ray spectrometers. *IEEE Trans. Nucl. Sci.* 57, 1654–1663. doi:10.1109/TNS.2010.2044809

De Siena, M. C., Klepov, V. V., Stepanoff, S. P., Bayikadi, K. S., Pan, L., Pandey, I. R., et al. (2023). Extreme γ -ray radiation tolerance of spectrometer-grade cspbbr3 perovskite detectors. *Adv. Mater.* 35, 2303244. doi:10.1002/adma.202303244

Dirin, D. N., Cherniukh, I., Yakunin, S., Shynkarenko, Y., and Kovalenko, M. V. (2016). Solution-grown cspbbr3 perovskite single crystals for photon detection. *Chem. Mater.* 28, 8470–8474. doi:10.1021/acs.chemmater.6b04298

Dönmez, B., He, Z., Kim, H., Cirignano, L. J., and Shah, K. S. (2012). Collection of holes in thick tlbr detectors at low temperature. *Nucl. Instrum. Methods Phys. Res. Sect. A Accel. Spectrom. Detect. Assoc. Equip.* 689, 7–11. doi:10.1016/j.nima.2012.06.020

Eisen, Y., Shor, A., and Mardor, I. (1999). Cdte and cdznte gamma ray detectors for medical and industrial imaging systems. *Nucl. Instrum. Methods Phys. Res. Sect. A Accel. Spectrom. Detect. Assoc. Equip.* 428, 158–170. doi:10.1016/S0168-9002(99)00003-0

Fano, U. (1947). Ionization yield of radiations. ii. the fluctuations of the number of ions. *Phys. Rev.* 72, 26–29. doi:10.1103/PhysRev.72.26

Feng, Y., Pan, L., Wei, H., Liu, Y., Ni, Z., Zhao, J., et al. (2020). Low defects density cspbbr3 single crystals grown by an additive assisted method for gamma-ray detection. *J. Mater. Chem. C* 8, 11360–11368. doi:10.1039/D0TC02706E

Frish, O. (1948). American and british atomic energy reports, br-149.

Gatti, E., and Rehak, P. (1984). Semiconductor drift chamber — an application of a novel charge transport scheme. *Nucl. Instrum. Methods Phys. Res.* 225, 608–614. doi:10.1016/0167-5087(84)90113-3

Han, Z., Mukherjee, A., Albert, A., Rumaiz, A., Harding, I., Tate, M., et al. (2023). High spatial resolution direct conversion amorphous selenium x-ray detectors with monolithically integrated cmos readout. *J. Instrum.* 18, P04021. doi:10.1088/1748-0221/18/04/P04021

Hansen, W. (1971). High-purity germanium crystal growing. *Nucl. Instrum. Methods* 94, 377–380. doi:10.1016/0029-554X(71)90593-3

He, Y., Matei, L., Jung, H. J., McCall, K. M., Chen, M., Stoumpos, C. C., et al. (2018). High spectral resolution of gamma-rays at room temperature by perovskite cspbbr3 single crystals. *Nat. Commun.* 9, 1609. doi:10.1038/s41467-018-04073-3

He, Y., Liu, Z., McCall, K. M., Lin, W., Chung, D. Y., Wessels, B. W., et al. (2019). Perovskite cspbbr3 single crystal detector for alpha-particle spectroscopy. *Nucl. Instrum. Methods Phys. Res. Sect. A Accel. Spectrom. Detect. Assoc. Equip.* 922, 217–221. doi:10.1016/j.nima.2019.01.008

He, Y., Petryk, M., Liu, Z., Chica, D. G., Hadar, I., Leak, C., et al. (2021). Cspbbr3 perovskite detectors with 1.4% energy resolution for high-energy γ-rays. *Nat. Photonics* 15, 36–42. doi:10.1038/s41566-020-00727-1

He, Y., Hadar, I., De Siena, M. C., Klepov, V. V., Pan, L., Chung, D. Y., et al. (2022). Sensitivity and detection limit of spectroscopic-grade perovskite cspbbr3 crystal for hard x-ray detection. *Adv. Funct. Mater.* 32, 2112925. doi:10.1002/adfm.202112925

Hitomi, K., Murayama, T., Shoji, T., Suehiro, T., and Hiratate, Y. (1999). Improved spectrometric characteristics of thallium bromide nuclear radiation detectors. *Nucl. Instrum. Methods Phys. Res. Sect. A Accel. Spectrom. Detect. Assoc. Equip.* 428, 372–378. doi:10.1016/S0168-9002(99)00141-2

Hull, E. L., Pehl, R. H., Lathrop, J. R., and Suttle, B. E. (2011). Yttrium hole-barrier contacts for germanium semiconductor detectors. *Nucl. Instrum. Methods Phys. Res. Sect. A Accel. Spectrom. Detect. Assoc. Equip.* 626-627, 39–42. doi:10.1016/j.nima.2010.10.029

Juška, G., and Arlauskas, K. (1980). Impact ionization and mobilities of charge carriers at high electric fields in amorphous selenium. *Phys. status solidi (a)* 59, 389–393. doi:10.1002/pssa.2210590151

Kabir, M. Z., and Hijazi, N. (2014). Temperature and field dependent effective hole mobility and impact ionization at extremely high fields in amorphous selenium. *Appl. Phys. Lett.* 104, 192103. doi:10.1063/1.4876239

Kanak, A., Kopach, O., Kanak, L., Levchuk, I., Isaiev, M., Brabec, C. J., et al. (2022). Melting and crystallization features of cspbbr3 perovskite. *Cryst. Growth & Des.* 22, 4115–4121. doi:10.1021/acs.cgd.1c01530

Kargar, A., Bolotnikov, A., Brown, C. A., Carini, G. A., Christian, J., Cirignano, L., et al. (2021). "Analysis of position-sensitive capacitive frisch-grid tlbr detectors," in *2021 IEEE nuclear science symposium and medical imaging conference* (NJ: United States NSS/MIC), 1–9. doi:10.1109/NSS/MIC44867.2021.9875535

Kargar, A., Christian, J. F., Bolotnikov, A., Pandey, I. R., Klepov, V., Zhang, W., et al. (2022). "Development of position-sensitive capacitive frisch-grid cspbbr3 detectors," in *2022 IEEE nuclear science symposium and medical imaging conference* (Italy: NSS/MIC), 1–6. doi:10.1109/NSS/MIC44845.2022.10399173

Kasap, S., Rowlands, J. A., Baranovskii, S. D., and Tanioka, K. (2004). Lucky drift impact ionization in amorphous semiconductors. *J. Appl. Phys.* 96, 2037–2048. doi:10.1063/1.1763986

Kasap, S., Frey, J. B., Belev, G., Tousignant, O., Mani, H., Laperriere, L., et al. (2009). Amorphous selenium and its alloys from early xeroradiography to high resolution x-ray image detectors and ultrasensitive imaging tubes. *Phys. status solidi (b)* 246, 1794–1805. doi:10.1002/pssb.200982007

Knoll, G. F. (2010). *Radiation detection and measurement; 4th edn.* New York, NY: Wiley.

Kolomiets, B. T., and Lyubin, V. M. (1973). Photoelectric phenomena in amorphous chalcogenide semiconductors. *Phys. status solidi (a)* 17, 11–46. doi:10.1002/pssa.2210170102

Kunar, D. A., Webster, M. F., Wu, Y., Kandel, R., and Wang, P. L. (2023). Development of single crystal cspbbr3 radiation detectors from low-cost solution synthesized material. *Crystals* 13, 762. doi:10.3390/cryst13050762

Li, J., Du, X., Niu, G., Xie, H., Chen, Y., Yuan, Y., et al. (2020). Rubidium doping to enhance carrier transport in cspbbr3 single crystals for high-performance x-ray detection. *ACS Appl. Mater. Interfaces* 12, 989–996. doi:10.1021/acsami.9b14772

Li, Z., Cheng, J., Liu, F., Wang, Q., Wen, W.-W., Huang, G., et al. (2024). Research on the technological progress of czt array detectors. *Sensors* 24, 725. doi:10.3390/s24030725

Luke, P. N., and Amman, M. (2007). Room-temperature replacement for ge detectors—are we there yet? *IEEE Trans. Nucl. Sci.* 54, 834–842. doi:10.1109/TNS.2007.903184

Malm, H. L. (1975). Properties of metal surface barriers on high purity germanium. *IEEE Trans. Nucl. Sci.* 22, 140–144. doi:10.1109/TNS.1975.4327631

[Dataset] McEnery, J., Barrio, J. A., Agudo, I., Ajello, M., Álvarez, J.-M., Ansoldi, S., et al. (2019). All-sky medium energy gamma-ray observatory: exploring the extreme multimessenger universe

Moiseev, A. A. (2021). New mission concept: galactic explorer with a coded aperture mask compton telescope (gecco) and its science perspectives

Mukherjee, A., Han, Z., Triet Ho, L. T., Rumaiz, A. K., Vasileska, D., and Goldan, A. H. (2023). Non-markovian hole excess noise in avalanche amorphous selenium thin films. *ACS Omega* 8, 23579–23586. doi:10.1021/acsomega.3c01256

Newville, M. (2014). Fundamentals of xafs. *Rev. Mineralogy Geochem.* 78, 33–74. doi:10.2138/rmg.2014.78.2

Nogami, M., Hitomi, K., Onodera, T., Watanabe, K., and Ishii, K. (2023). Reversible capacitive frisch grid tlbr detectors. *Jpn. J. Appl. Phys.* 62, 096501. doi:10.35848/1347-4065/acf0aa

Nygren, D. R. (1975). "A time projection chamber: 1975," in *1975 PEP summer study*, 126–133.

Ohsugi, T., Yoshida, S., Fukazawa, Y., Yamamura, K., Sato, K., Yamamoto, K., et al. (2005). Design and properties of the glast flight silicon micro-strip sensors. *Nucl. Instrum. Methods Phys. Res. Sect. A Accel. Spectrom. Detect. Assoc. Equip.* 541, 29–39. doi:10.1016/j.nima.2005.01.035

Palleti, P. C., Seyidov, P., Gybin, A., Pietsch, M., Juda, U., Fiedler, A., et al. (2024). Properties of a highly compensated high-purity germanium. *J. Mater. Sci. Mater. Electron.* 35, 57. doi:10.1007/s10854-023-11814-8

Pan, L., Feng, Y., Kandlakunta, P., Huang, J., and Cao, L. R. (2020). Performance of perovskite cspbbr3 single crystal detector for gamma-ray detection. *IEEE Trans. Nucl. Sci.* 67, 443–449. doi:10.1109/TNS.2020.2964306

Peng, J., Xia, C. Q., Xu, Y., Li, R., Cui, L., Clegg, J. K., et al. (2021). Crystallization of cspbbr3 single crystals in water for x-ray detection. *Nat. Commun.* 12, 1531. doi:10.1038/s41467-021-21805-0

Philipp, H. T., Tate, M. W., Purohit, P., Shanks, K. S., Weiss, J. T., and Gruner, S. M. (2016). High-speed x-ray imaging pixel array detector for synchrotron bunch isolation. *J. Synchrotron Radiat. (Online)* 23, 395–403. doi:10.1107/s1600577515022754

Philipp, H. T., Tate, M. W., Shanks, K. S., Purohit, P., and Gruner, S. M. (2020). High dynamic range cdte mixed-mode pixel array detector (mm-pad) for kilohertz imaging of hard x-rays. *J. Instrum.* 15, P06025. doi:10.1088/1748-0221/15/06/p06025

Polack, J., Hirt, M., Sturgess, J., Sferrazza, N., Bolotnikov, A., Babalola, S., et al. (2010). Variation of electric shielding on virtual frisch-grid detectors. *Nucl. Instrum. Methods Phys. Res. Sect. A Accel. Spectrom. Detect. Assoc. Equip.* 621, 424–430. doi:10.1016/j.nima.2010.05.035

Protic, D., and Riepe, G. (1985). Position-sensitive germanium detectors. *IEEE Trans. Nucl. Sci.* 32, 553–555. doi:10.1109/TNS.1985.4336893

Protic, D., Stohlker, T., Krings, T., Mohos, I., and Spillmann, U. (2005). Two-dimensional microstrip germanium detector for the spectroscopy of hard x-ray transitions. *IEEE Trans. Nucl. Sci.* 52, 3194–3198. doi:10.1109/TNS.2005.862932

Qin, H., Xiao, B., He, X., Ouyang, X., Gao, T., Wang, Y., et al. (2025). Virtual frisch grid perovskite cspbbr3 semiconductor with 2.2-centimeter thickness for high energy resolution gamma-ray spectrometer. *Nat. Commun.* 16, 158. doi:10.1038/s41467-024-55561-8

Rakita, Y., Kedem, N., Gupta, S., Sadhanala, A., Kalchenko, V., Böhm, M. L., et al. (2016). Low-temperature solution-grown cspbbr3 single crystals and their characterization. *Cryst. Growth & Des.* 16, 5717–5725. doi:10.1021/acs.cgd.6b00764

Rubel, O., Baranovskii, S. D., Zvyagin, I. P., Thomas, P., and Kasap, S. O. (2004). Lucky-drift model for avalanche multiplication in amorphous semiconductors. *Phys. status solidi C.* 1, 1186–1193. doi:10.1002/pssc.200304319

Rumaiz, A. K., Krings, T., Siddons, D. P., Kuczewski, A. J., Protic, D., Ross, C., et al. (2014). A monolithic segmented germanium detector with highly integrated readout. *IEEE Trans. Nucl. Sci.* 61, 3721–3726. doi:10.1109/TNS.2014.2365358

Rumaiz, A. K., Weiland, C., Harding, I., Nooman, N. S., Krings, T., Hull, E. L., et al. (2023). Interface formation and schottky barrier height for y, nb, au, and pt on ge as

determined by hard x-ray photoelectron spectroscopy. *AIP Adv.* 13, 015305. doi:10.1063/5.0101688

Schein, L. B. (1974). Charge generation from band-gap states in amorphous selenium films. *Phys. Rev. B* 10, 3451–3457. doi:10.1103/PhysRevB.10.3451

Scott, C. C., Farrier, M., Li, Y., Laxer, S., Ravi, P., Kenesei, P., et al. (2021). High-energy micrometre-scale pixel direct conversion X-ray detector. *J. Synchrotron Radiat.* 28, 1081–1089. doi:10.1107/S1600577521004835

Stoumpos, C. C., Malliakas, C. D., Peters, J. A., Liu, Z., Sebastian, M., Im, J., et al. (2013). Crystal growth of the perovskite semiconductor cspbbr3: a new material for high-energy radiation detection. *Cryst. Growth & Des.* 13, 2722–2727. doi:10.1021/cg400645t

Szeles, C. (2004). CdZnTe and CdTe materials for X-ray and gamma ray radiation detector applications. *IEEE Trans. Nucl. Sci.* 51, 1175–1183. doi:10.1002/pssb.200304296

Tanioka, K., Yamazaki, J., Shidara, K., Taketoshi, K., Kawamura, T., Ishioka, S., et al. (1987). An avalanche-mode amorphous selenium photoconductive layer for use as a camera tube target. *IEEE Electron Device Lett.* 8, 392–394. doi:10.1109/EDL.1987.26671

Toufanian, R., Swain, S., Becla, P., Motakef, S., and Datta, A. (2022). Cesium lead bromide semiconductor radiation detectors: crystal growth, detector performance and polarization. *J. Mater. Chem. C* 10, 12708–12714. doi:10.1039/D2TC01679F

Valverde, J., Kirschner, N., Metzler, Z., Smith, L. D., Cannady, N. W., Caputo, R., et al. (2023). The compton pair telescope: a prototype for a next-generation mev gamma-ray observatory. *Proc. 38th Int. Cosmic Ray Conf. — PoS(ICRC2023)* 857, 857. doi:10.22323/1.444.0857

Vernon, E., Geronimo, G. D., Baldwin, J., Chen, W., Fried, J., Giacomini, G., et al. (2019). Development of a high rate front-end asic for x-ray spectroscopy and diffraction applications.

Vernon, E., De Geronimo, G., Baldwin, J., Chen, W., Fried, J., Giacomini, G., et al. (2020). Development of a high-rate front-end asic for x-ray spectroscopy and diffraction applications. *IEEE Trans. Nucl. Sci.* 67, 752–759. doi:10.1109/TNS.2020.2976820

Wang, F., Bai, R., Sun, Q., Liu, X., Cheng, Y., Xi, S., et al. (2022). Precursor engineering for solution method-grown spectroscopy-grade cspbbr3 crystals with high energy resolution. *Chem. Mater.* 34, 3993–4000. doi:10.1021/acs.chemmater.2c00071

Watanabe, K., Sugai, Y., Hasegawa, S., Tanaka, S., Hitomi, K., Nogami, M., et al. (2024). Comparison between carrier transport property and crystal quality of tlbr semiconductors. *Sci. Rep.* 14, 25224. doi:10.1038/s41598-024-76005-9

Wu, R., Kang, Y., Wei, D., Fan, D., Li, Y., Wu, S., et al. (2022). Energy spectrum correction and carrier mobility calculation of cdznte pixel detector based on the depth of interaction. *IEEE Trans. Nucl. Sci.* 69, 1773–1779. doi:10.1109/TNS.2022.3170427

Zhang, H., Liu, X., Dong, J., Yu, H., Zhou, C., Zhang, B., et al. (2017). Centimeter-sized inorganic lead halide perovskite cspbbr3 crystals grown by an improved solution method. *Cryst. Growth & Des.* 17, 6426–6431. doi:10.1021/acs.cgd.7b01086

Zhang, M., Zheng, Z., Fu, Q., Chen, Z., He, J., Zhang, S., et al. (2018). Synthesis and single crystal growth of perovskite semiconductor cspbbr3. *J. Cryst. Growth* 484, 37–42. doi:10.1016/j.jcrysgro.2017.12.020

Zhang, B.-B., Wang, F., Zhang, H., Xiao, B., Sun, Q., Guo, J., et al. (2020a). Defect proliferation in cspbbr3 crystal induced by ion migration. *Appl. Phys. Lett.* 116, 063505. doi:10.1063/1.5134108

Zhang, H., Wang, F., Lu, Y., Sun, Q., Xu, Y., Zhang, B.-B., et al. (2020b). High-sensitivity x-ray detectors based on solution-grown caesium lead bromide single crystals. *J. Mater. Chem. C* 8, 1248–1256. doi:10.1039/C9TC05490A

Zhang, P., Sun, Q., Xu, Y., Li, X., Liu, L., Zhang, G., et al. (2020c). Enhancing carrier transport properties of melt-grown cspbbr3 single crystals by eliminating inclusions. *Cryst. Growth & Des.* 20, 2424–2431. doi:10.1021/acs.cgd.9b01616

Zhang, X., Li, F., Bai, R., Sun, Q., Hao, Y., Xi, S., et al. (2022). Investigation on energy resolution of cspbbr3 detectors: from charge transport behavior to device configuration. *J. Mater. Chem. C* 10, 6017–6024. doi:10.1039/D2TC00566B

Zhang, X., Li, F., Hao, Y., Bai, R., Xin, Y., Sun, Q., et al. (2023). Improved energy resolution by weighting potential optimization in cspbbr3 pixelated gamma-ray detector. *IEEE Trans. Electron Devices* 70, 5190–5195. doi:10.1109/TED.2023.3307506

Zhao, W., and Rowlands, J. A. (1995). X-ray imaging using amorphous selenium: feasibility of a flat panel self-scanned detector for digital radiology. *Med. Phys.* 22, 1595–1604. doi:10.1118/1.597628

Zhao, B., and Zhao, W. (2008). Imaging performance of an amorphous selenium digital mammography detector in a breast tomosynthesis system. *Med. Phys.* 35, 1978–1987. doi:10.1118/1.2903425